SANDIA REPORT

SAND91—0862 • UC—233
Unlimited Release
Printed June 1991

Structural Analysis of a Reflux Pool-Boiler Solar Receiver

Edward L. Hoffman, Charles M. Stone

Prepared by
Sandia National Laboratories
Albuquerque, New Mexico 87185 and Livermore, California 94550
for the United States Department of Energy
under Contract DE-AC04-76DP00789

Issued by Sandia National Laboratories, operated for the United States Department of Energy by Sandia Corporation.

Available to DOE and DOE contractors from
Office of Scientific and Technical Information
PO Box 62
Oak Ridge, TN 37831

Prices available from (615) 576-8401, FTS 626-8401

Available to the public from
National Technical Information Service
US Department of Commerce
5285 Port Royal Rd
Springfield, VA 22161

NTIS price codes
Printed copy: A03
Microfiche copy: A01

SAND91-0862
Unlimited Release
Printed June, 1991

SAND--91-0862

DE92 002211

Structural Analysis of a Reflux Pool-Boiler Solar Receiver

Edward L. Hoffman
Charles M. Stone

Engineering and Structural Mechanics Division
Sandia National Laboratories
Albuquerque, New Mexico 87185

Abstract

Coupled thermal-structural finite element calculations of a reflux pool-boiler solar receiver were performed to characterize the operating stresses and to address issues affecting the service life of the receiver. Analyses performed using shell elements provided information for receiver material selection and design optimization. Calculations based on linear elastic fracture mechanics principles were performed using continuum elements to assess the vulnerability of a seam-weld to fatigue crack growth. All calculations were performed using ABAQUS, a general purpose finite element code, and elements specifically formulated for coupled thermal-structural analysis. Two materials were evaluated: 316L SS and Haynes 230 alloys. The receiver response was simulated for a combination of structural and thermal loads that represent the startup and operating conditions of the receiver. For both materials, maximum stresses in the receiver developed shortly after startup due to uneven temperature distribution across the receiver surface. The largest effective stress was near yield in the 316L SS receiver and below 39 percent of yield in the Haynes 230 receiver. The calculations demonstrated that significant stress reductions (over 25 percent) could be obtained by reducing the aft dome thickness to one closer to the absorber. The fatigue calculations demonstrated that the stress distribution near the seam-weld notch depends primarily on the structural load created by internal pressurization of the receiver rather than the thermal loads, indicating that the thermal loads can be neglected when assessing the stress intensity near the seam-weld notch. The stress intensity factor, computed using the J-integral method and crack opening-displacement field equations, was shown to be significantly below the fatigue threshold for most steels. Furthermore, the calculations indicated that the weld notch was always loaded in compression, a condition which is not conducive to fatigue crack growth.

Acknowledgments

The authors would like to acknowledge G. W. Wellman for his generous support and guidance in the fracture mechanics aspects of this analysis.

Contents

Figures

Tables

1 Introduction

Sandia National Laboratories, together with the U. S. Department of Energy, has identified Stirling Dish-Electric systems as having potential to meet long-term program goals in solar energy [1]. In the solar dish-electric concept, a receiver absorbs energy reflected from a parabolic mirror which tracks the sun. Thermal energy from the receiver is used to drive an engine, which powers an electric generator. Many types of conversion devices have been considered for dish-electric systems; however, the Stirling engine is of greatest interest because it has exceptionally high thermodynamic efficiency [2]. The term *reflux* is used to describe the method by which thermal energy is transferred to the Stirling engine. In a reflux receiver, a liquid metal functions as an intermediate heat transfer fluid between the solar absorber and the heater tubes of the Stirling engine. This intermediate fluid is contained in an evacuated vessel and vaporized from the backside of the solar absorber. The vapor condenses on the Stirling engine heat tubes, releasing the latent heat, and then passively returns to the backside of the solar absorber due to gravity (refluxing). Pool-boiling assures that there is sufficient inventory of liquid metal to completely wet the absorber surface and establish a convective current.

A prototype sodium reflux pool-boiler receiver, developed at Sandia National Laboratories by the Solar Thermal Electric Technology Division (6217), was recently tested on-sun. Figure 1 is a schematic of the Sandia-developed reflux pool-boiler receiver. The solar receiver dish consists of two 316L stainless steel spherical domes, the absorber and aft-dome, edge-welded together to form a hermetically sealed hollow dish. The space between the absorber and aft-dome contains liquid sodium. The receiver's sodium inventory of 12.7 pounds ensures that the entire absorber surface will be wetted in all dish orientations. During current on-sun testing, the Stirling engine has been replaced by a cold water calorimeter for controlled heat extraction. The operating environment exposes the receiver to transient temperatures ranging from 20 °C to 820 °C. The loading is cyclic with at least 10,000 startup/shutdown cycles expected during the design lifetime. In addition to the thermal loads, the receiver is subject to a cyclic change in internal pressure between zero and one-half atmosphere absolute. The receiver must contain the liquid sodium which will burn when exposed to air. Detailed knowledge of the thermal stresses induced in the absorber is needed to design the receiver to operate for its 30-year lifetime.

As an intermediate step in the development of a next-generation receiver, two changes in the original design have been considered: using Haynes 230 alloy which is more creep resistant than 316L stainless steel, and replacing the edge-weld with a seam-weld. Design requirements of this intermediate design include maximizing thermal efficiency while optimizing structural performance and component life. The Solar Thermal Electric Technology Division requested that the Engineering and Structural Mechanics Division (1514) provide structural analysis support for the reflux pool-boiler receiver project. Coupled temperature-displacement analyses have been performed for receiver material selection, design optimization, and issues that affect the lifetime of the receiver [3,4,5,6]. All calculations were performed using ABAQUS, a general purpose finite element code, and elements specifically formulated for coupled thermal-structural analysis [7]. Analyses performed using shell elements provided information for re-

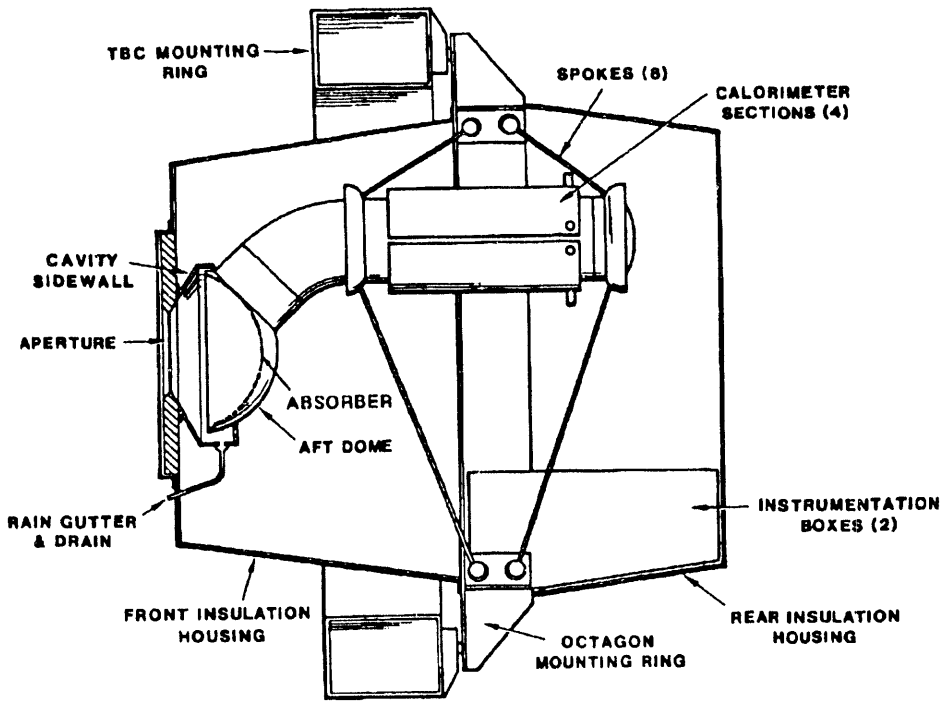

Figure 1. Schematic of the reflux pool-boiler receiver [8].

ceiver material selection and design optimization. Calculations based on linear elastic fracture mechanics principles were performed using continuum elements to assess the vulnerability of the proposed seam-weld to fatigue crack growth. These analyses, coupled with results of developmental testing, are intended to assess the performance of the prototype receiver and to assist in the development of a next-generation receiver.

This report documents and summarizes the results of structural analyses performed for and presented to the Solar Thermal Electric Technology Division. The next section provides a general description of the problem, including geometrical assumptions, material properties, and boundary conditions. Section 3 presents coupled thermal-structural analyses performed with shell elements. These calculations characterize the overall receiver stresses and address optimization issues. A critical issue in assessing the life of the receiver is the fatigue strength of the seam weld which joins the absorber and aft dome [9]. Section 4 presents a more detailed fatigue analysis of this seam-weld. Finally, conclusions and recommendations are presented in Section 5.

2 Problem Definition

2.1 Problem Geometry

Figure 2 shows the idealized geometry and dimensions used for modeling the reflux pool-boiler receiver. The receiver model consists of the absorber, which is a spherical dome with a 219-mm radius and a 70.2-degree half angle, and the aft dome which is another spherical dome with a 208-mm radius. The design gap between the domes is nominally 34.3 mm. The thickness of the absorber is 0.813 mm compared to 3.18 mm for the aft dome. In the prototype receiver, the absorber is edge-welded to the aft dome around its outer circumference. A seam-weld has been proposed as a change to the original design.

The receiver assembly is supported by a 203-mm-diameter pipe (see Figure 1) designed to mate with a cold water calorimeter for controlled power extraction. Since the primary interest was in receiver response to thermal loads, the pipe mount was not included in the finite element models. There is no differential expansion between these components because the support pipe is constructed of the same material as the receiver. However, the bending moment imposed by the support pipe on the aft dome is neglected in this simplification. This assumption allowed for an axisymmetric representation of the receiver.

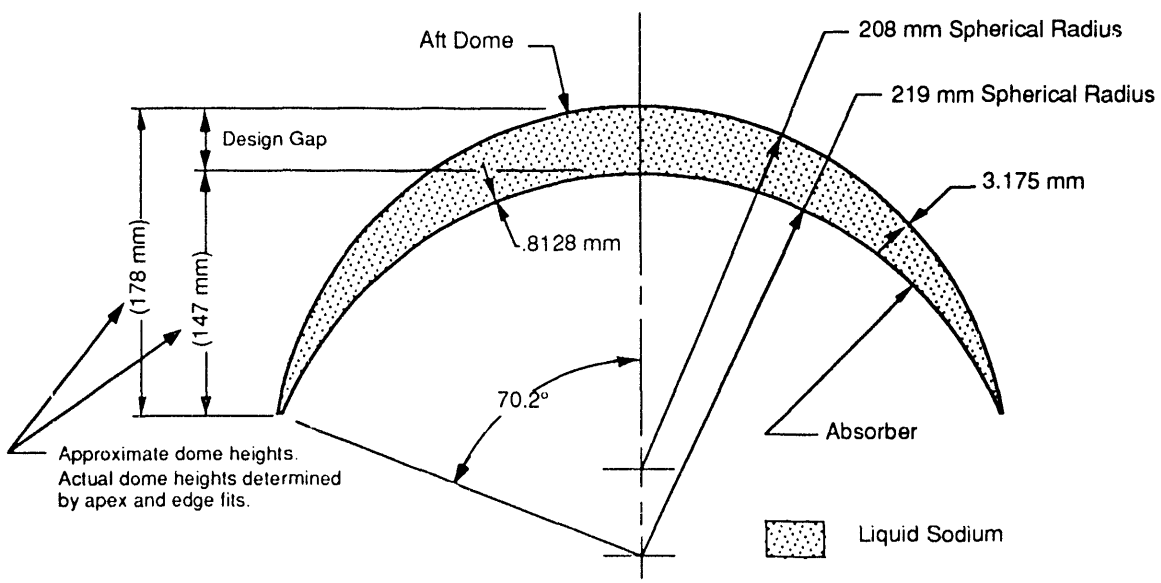

Figure 2. Geometric detail of the reflux pool-boiler receiver.

2.2 Material Properties

The prototype receiver currently undergoing on-sun testing is constructed of 316L stainless steel, but plans call for a next-generation receiver to be constructed of Haynes 230 steel which is more creep resistant than 316L SS. Both materials were modeled as linear-elastic with temperature dependent material properties. The material properties, specified as functions of temperature, are the elastic modulus presented in Table 1, the thermal conductivity in Table 2, and the coefficient of thermal expansion in Table 3. A temperature independent Poisson's ratio of 0.3 was used for both alloys, and yield stresses of 103 and 260 MPa were used for 316L SS and Haynes 230 at 800 °C, respectively.

2.3 Structural Boundary Conditions

The structural boundary conditions used in the analyses are shown schematically in Figure 3a. Radial displacements of the absorber and aft dome are specified to be zero at the axis of symmetry. The centerline node on the back surface of the aft dome is constrained in both the axial and radial directions to remove axial rigid body deformation from the problem. The coordinate *s*, denoting surface position on the receiver and aft dome, is defined in Figure 3b. This parameter will be used later for presentation of temperature data and analysis results.

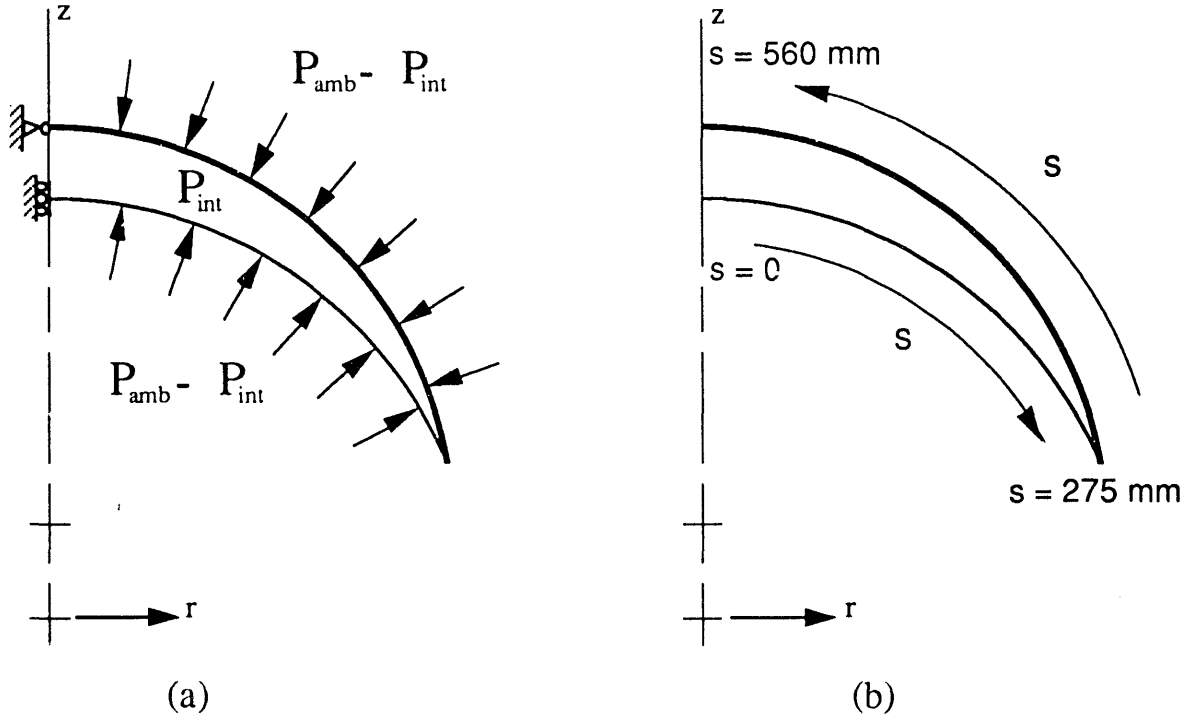

Figure 3. (a) Structural boundary conditions used for the reflux pool-boiler receiver analyses. (b) Definition of the surface position variable, *s*, used for the presentation of results.

Table 1. Temperature Dependent Elastic Moduli Used for the Pool-Boiler Receiver Analyses.

Temperature (°C)	316L Elastic Modulus (GPa)	Haynes 230 Elastic Modulus (GPa)
100	190.1	207
200	184.0	202
300	176.7	196
400	168.3	190
500	159.9	184
600	149.1	177
700	138.6	171
800	126.1	164

Table 2. Temperature Dependent Thermal Conductivity Used for the Pool-Boiler Receiver Analyses.

Temperature (°C)	316L Conductivity (W/m K)	Haynes 230 Conductivity (W/m K)
100	14.7	10.4
200	16.34	12.4
300	17.94	14.4
400	19.48	16.4
500	20.96	18.4
600	22.39	20.4
700	23.76	22.4
800	25.07	24.4

Table 3. Temperature Dependent Coefficient of Thermal Expansion Used for the Pool-Boiler Receiver Analyses.

Temperature (°C)	316L Coefficient of Thermal Expansion ($\times 10^{-6}$ °C $^{-1}$)	Haynes 230 Coefficient of Thermal Expansion ($\times 10^{-6}$ °C $^{-1}$)
100	15.8	12.7
200	16.7	13.0
300	17.2	13.3
400	17.8	13.7
500	18.3	14.0
600	18.6	14.4
700	18.9	14.8
800	19.2	15.2

To represent loading induced by the pressure differential between the liquid sodium and the surrounding atmosphere, a uniform pressure boundary condition was applied to the aft dome and absorber as shown in Figure 3a. The external pressure, P_{amb}, represents the local ambient pressure (84.1 kPa in Albuquerque, NM), while P_{int} is the absolute pressure of the liquid sodium given by the following equation [10]

$$\log P_{int} = 6.354 - \frac{5567}{T} - 0.5 \log T \tag{1}$$

where T is the sodium absolute temperature in Kelvin (K) and P_{int} is in standard atmospheres. According to Equation (1), the internal pressure, P_{int}, is zero absolute at ambient temperature (300 K) and increases with increasing temperature. Consequently, the applied pressure (P_{amb}-P_{int}) is initially 84.1 kPa (approximately 1 atm.) when the receiver is off-sun, and decreases to an on-sun steady state value of 32.9 kPa (approximately 0.5 atm.) at 800 °C.

2.4 Thermal Boundary Conditions

The thermal model of the receiver utilizes temperature data taken from thermocouples at discrete points on the outer surfaces of the absorber and aft dome as well as a computed incident solar flux distribution. The absorber thermocouple data have not been corrected for the effect of the incident solar flux, and are estimated to be up to 20 °C higher than the absorber temperature, depending on the flux level. The convention illustrated in Figure 4 is used to denote the two sides of the aft dome and the absorber shells. The *inner* surfaces of the shells are in contact with the liquid sodium (internal to the sodium containment), while the *outer* surfaces are exposed to the atmosphere. During startup (Figure 4a), temperatures are defined on the *outer* surface of the absorber where they were measured, and the solar flux is applied on the *inner* surface where the temperatures were not known. Aft dome temperatures, also measured on the *outer* surface of the receiver, are assumed constant through the shell thickness. The assumed temperature profile of the receiver, shown in Figure 5, is based on temperature data measured at six discrete locations on the prototype receiver. The data are presented as a function of the surface distance coordinate *s* defined in Figure 3b. Each temperature data point represents the average of four measurements made at 90° intervals at the same surface position on the receiver. The temperature data were linearly interpolated between the data points. The spatially varying flux distribution, shown in Figure 6, was calculated using CIRCE2 [11], a computer code for calculating incident solar flux distributions of point-focus concentrators. For each absorber element, the flux data were entered into the analysis as a function of the radial coordinate of the element. The sodium temperature used to calculate the internal pressure in Equation (1) was assumed equal to the temperature at the aft dome axis of symmetry.

When steady state operating conditions are reached (Figure 4b), a constant temperature boundary condition of 811.5 °C is specified on the *inner* surface of the absorber, and the spatially varying flux distribution in Figure 6 is specified on the *outer* surface of the absorber. The temperature specification during this phase of operation was moved to the *inner* surface

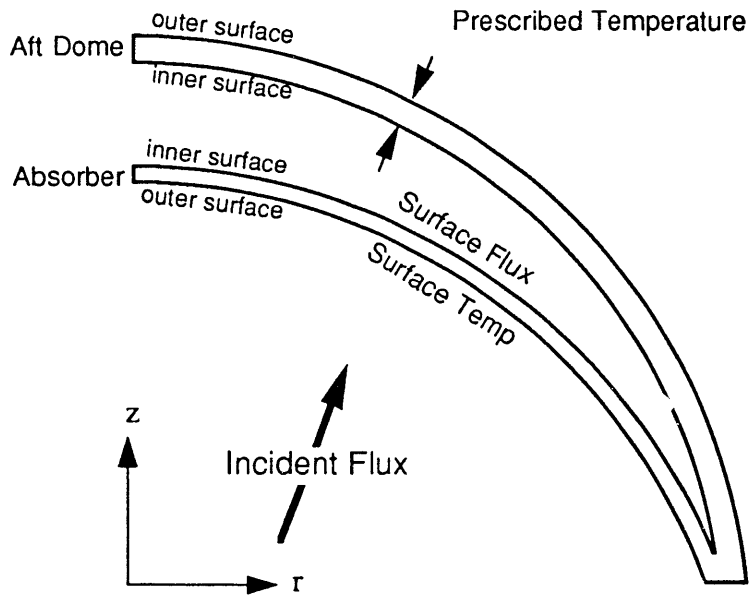

(a) Startup Phase

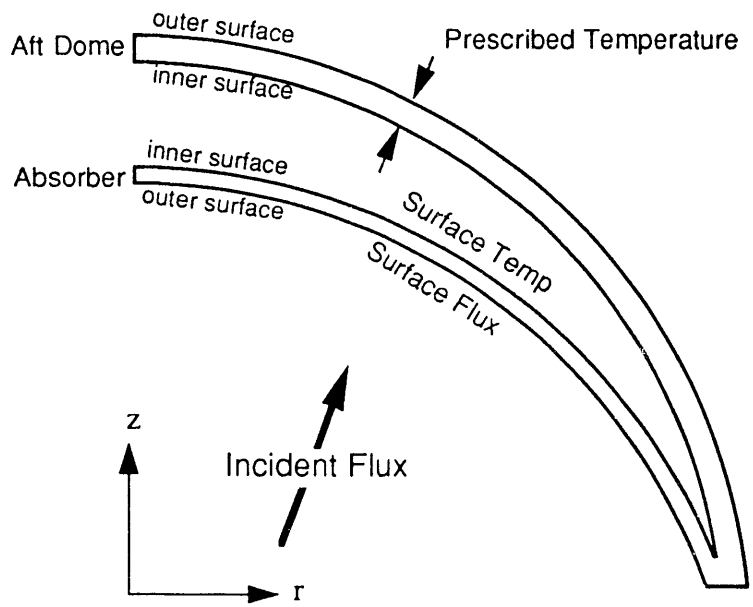

(a) Steady State Phase

Figure 4. Thermal boundary conditions used for the reflux pool-boiler receiver analysis.

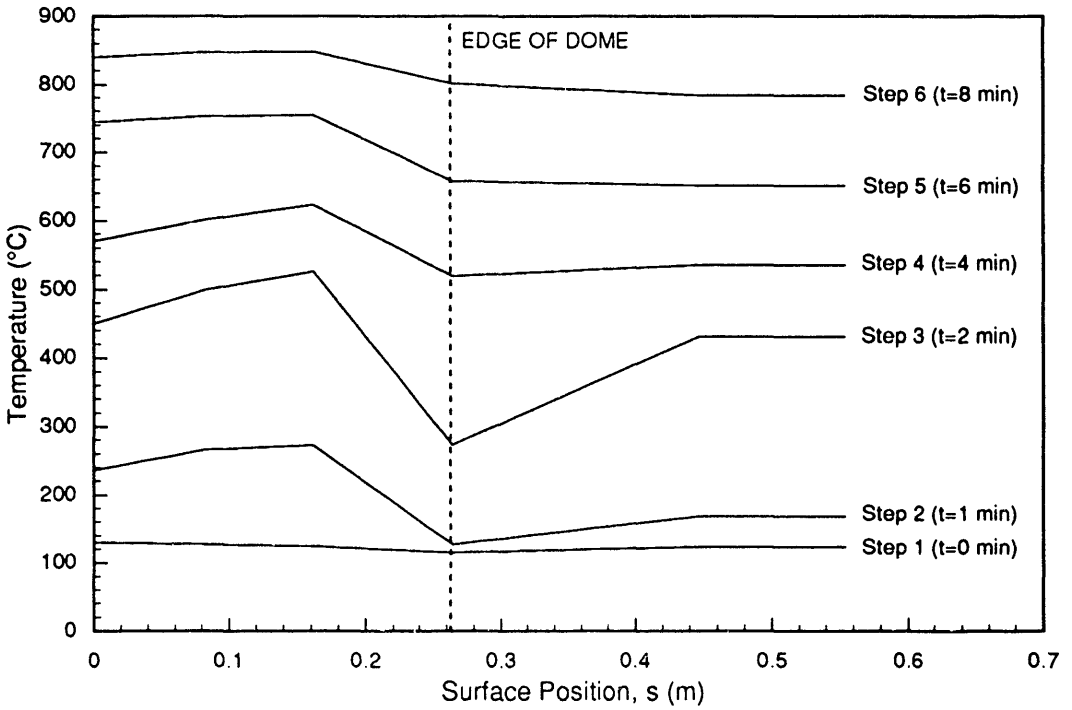

Figure 5. Assumed absorber and aft dome *outer* surface temperature profiles as a function of surface position (see Figure 3b) for startup operating conditions.

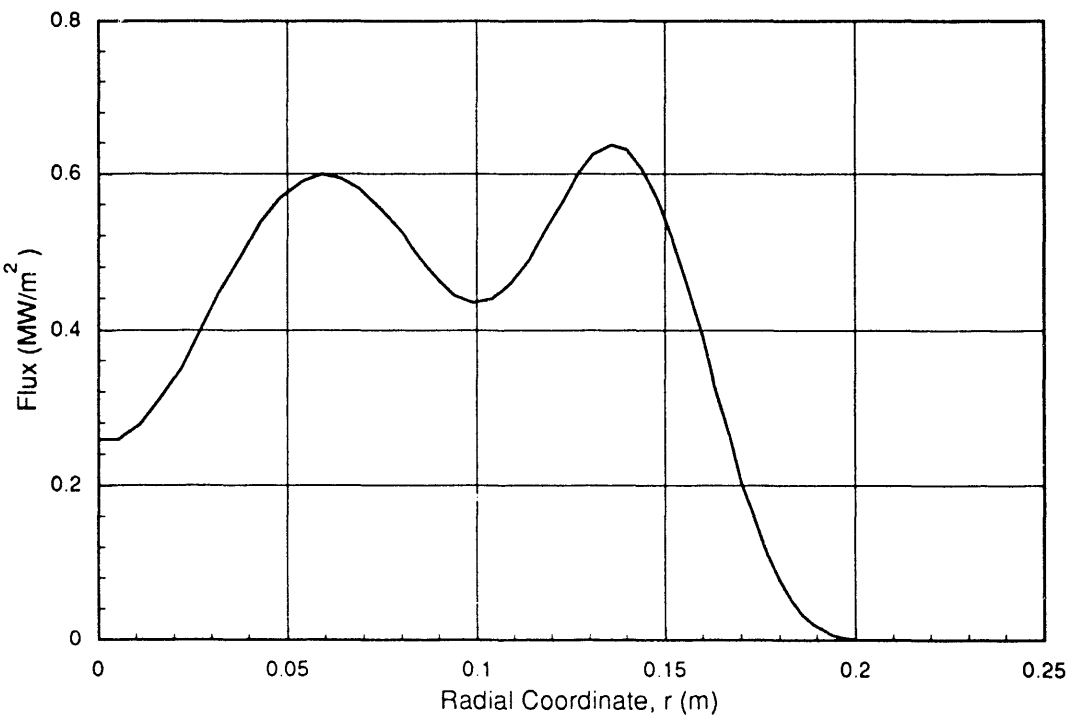

Figure 6. Computed incident solar flux distribution assumed for the startup and steady state operating conditions as a function of the radial coordinate of the receiver.

because an estimate of the wall temperature can be made at the sodium/wall interface based on the measured bulk sodium temperature (assumed to be uniform) and the estimated wall superheat. The aft dome is subjected to a constant temperature boundary condition of 811.5 °C through the thickness of the shell.

3 Shell Analyses of Receiver

Coupled thermal-structural calculations were performed with an axisymmetric shell model of the receiver. The calculations were performed to characterize the stress generated by heating the receiver during startup and steady state operation. Both 316L SS and Haynes 230 were considered. Furthermore, the same model was used to investigate the effects of aft dome thickness reductions in a Haynes 230 receiver. Reducing the aft dome thickness would result in a significant savings in material costs. The analyses were performed for both startup and steady state phases of operation. The following sections present the details of the finite element model, the receiver material assessment calculations, and the aft dome optimization study.

3.1 Details of Finite Element Analyses

The geometry assumptions and load conditions discussed in the preceding section allowed the use of an axisymmetric model of the receiver. The model was constructed using 80 three-noded axisymmetric shell elements developed specifically for coupled thermal-structural analyses. These elements use quadratic interpolation for the geometry and displacements while the temperatures are linearly interpolated from the end nodes and piecewise quadratically through the shell thickness. Five integration points through the shell thickness were specified for all calculations.

During startup, the six temperature distributions shown in Figure 5 were individually and sequentially applied and the solutions were obtained independently as quasi-steady state solutions. The steady state operating phase of the receiver is analyzed as a seventh steady state solution. The quasi-steady state assumption is appropriately based on the thermal diffusivity of the material, the absorber wall thickness, and the relatively long times involved in the startup process. The receiver reacts much more rapidly to transient external conditions compared to the time required to start the receiver (9 minutes). As a result, transient effects are negligible. For each solution, the thermal strains are calculated from an initial reference temperature of 20 °C.

3.2 Receiver Material Assessment

Although each nodal point has temperatures computed at five points through the shell, only the temperatures at the *inner* and *outer* surfaces are presented for all seven time steps. In addition, stress output from the axisymmetric shell elements is provided in the form of meridional and circumferential stresses at the *inner* and *outer* surfaces. The stress results are presented for Steps 3 and 7 for each analysis because the largest stresses are generated at Step 3 of startup, and Step 7 corresponds to steady state on-sun operation. Both the temperature and stress results are presented as a function of the surface distance coordinate, s, defined in Figure 3b.

3.2.1 316L SS Receiver

The nodal temperatures computed along the *inner* and *outer* surfaces of the 316L SS receiver are shown in Figure 7 and Figure 8, respectively. Curves 1 through 6 correspond to the startup thermal profiles and Curve 7 corresponds to the steady state temperature distribution. The curves in Figure 7 for s greater than 0.266 m and the complete curves in Figure 8 agree with the input temperatures shown in Figure 4. The *inner* surface temperatures shown in Figure 7 for $s < 0.266$ m show only slight variations from the prescribed temperatures. This indicates that the temperature gradients through the thickness are small.

The meridional and circumferential stress distributions in the 316L SS receiver are shown in Figure 9 and Figure 10 for Steps 3 and 7, respectively. The meridional and the circumferential stress profiles are nearly equal. As a result, the effective von Mises stress are of similar magnitude to the individual components and are therefore not presented. The absorber shell is subjected to nearly pure bending with the *inner* surface of the shell in tension and the *outer* surface in compression. The stress magnitudes exceed 100 MPa. The bending response is due to the differential thermal expansion through the wall thickness caused by the temperature gradient. Large stress gradients occur near the junction of the absorber and aft dome due to the difference between the average temperatures of the absorber and aft dome and the geometric discontinuity which exists between the shell thicknesses at this location. The effective stress is very close to the 103 MPa yield strength of 316L SS. Membrane stresses in the receiver are characterized by an offset from zero in the average meridional and circumferential stress components. This membrane stress is tensile in the absorber and compressive in the aft dome.

At steady state operating conditions, the *inner* surface remains in tension, and the *outer* surface remains in compression with the maximum tensile and compressive stresses reduced to 42 MPa and -33 MPa, respectively. The meridional and circumferential stresses for the *outer* surface are almost identical and overlap in Figure 10. The stress profiles exhibit the distinctive double hump characteristic of the incident solar flux distribution shown in Figure 6. Near the absorber edge, the stress components are only 10 MPa because the surface temperature of the receiver is more uniform during steady state operation. At steady state, the edge stress gradient is due primarily to the geometric discontinuity which exists at the absorber/aft dome interface.

3.2.2 Haynes 230 Receiver

The temperatures generated on the *inner* and *outer* surfaces of the Haynes 230 receiver were practically the same as those discussed for the 316L SS receiver. As a result, they are not presented. The similarity was not surprising since the thermal properties of the two materials are so similar. The comments made regarding the temperature distribution for the 316L SS receiver are still valid for this receiver material.

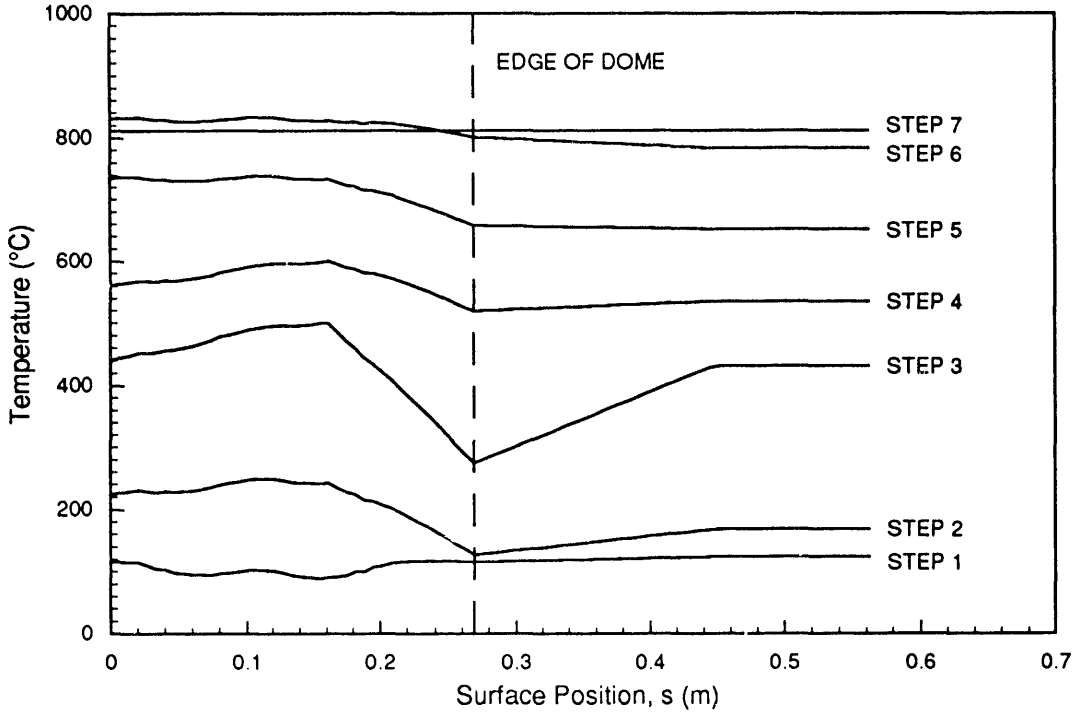

Figure 7. Absorber and aft dome *inner* temperature profiles for startup and steady state operating conditions.

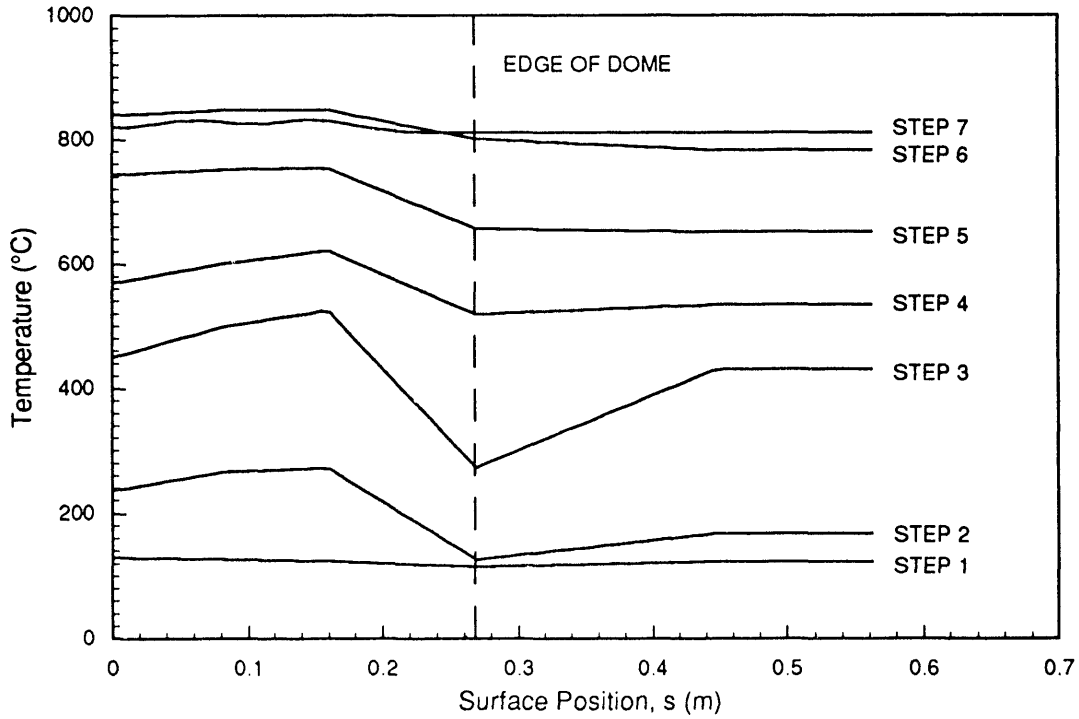

Figure 8. Absorber and aft dome *outer* temperature profiles for startup and steady state operating conditions.

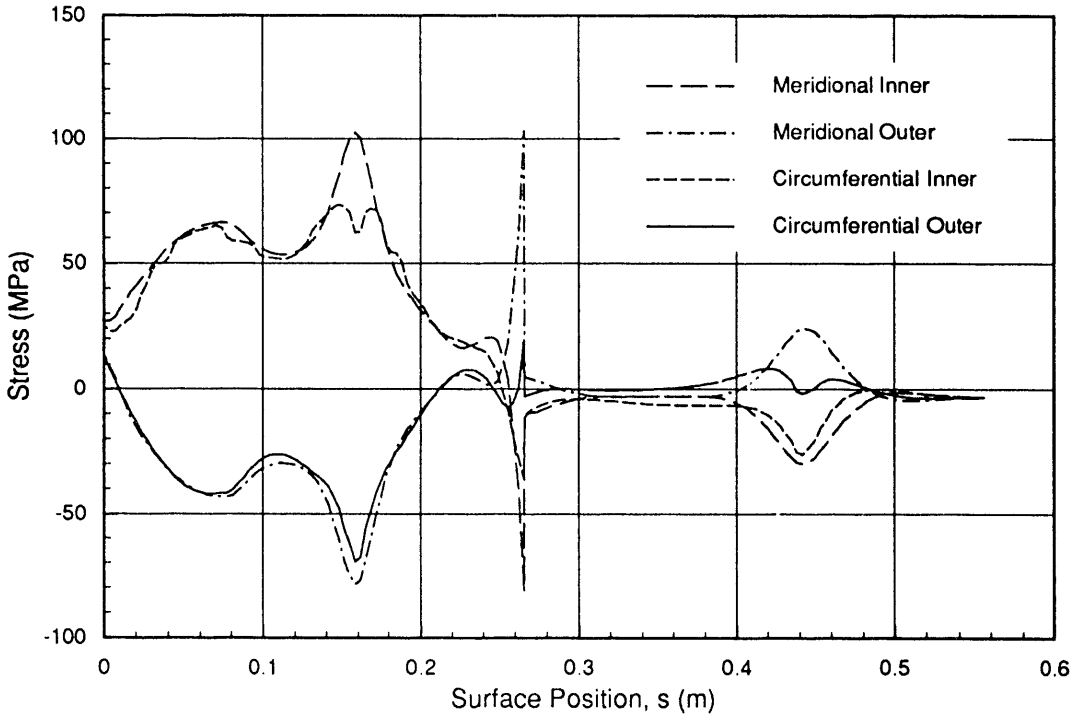

Figure 9. Receiver meridional and circumferential stress profiles during Step 3 of the receiver startup for 316L SS.

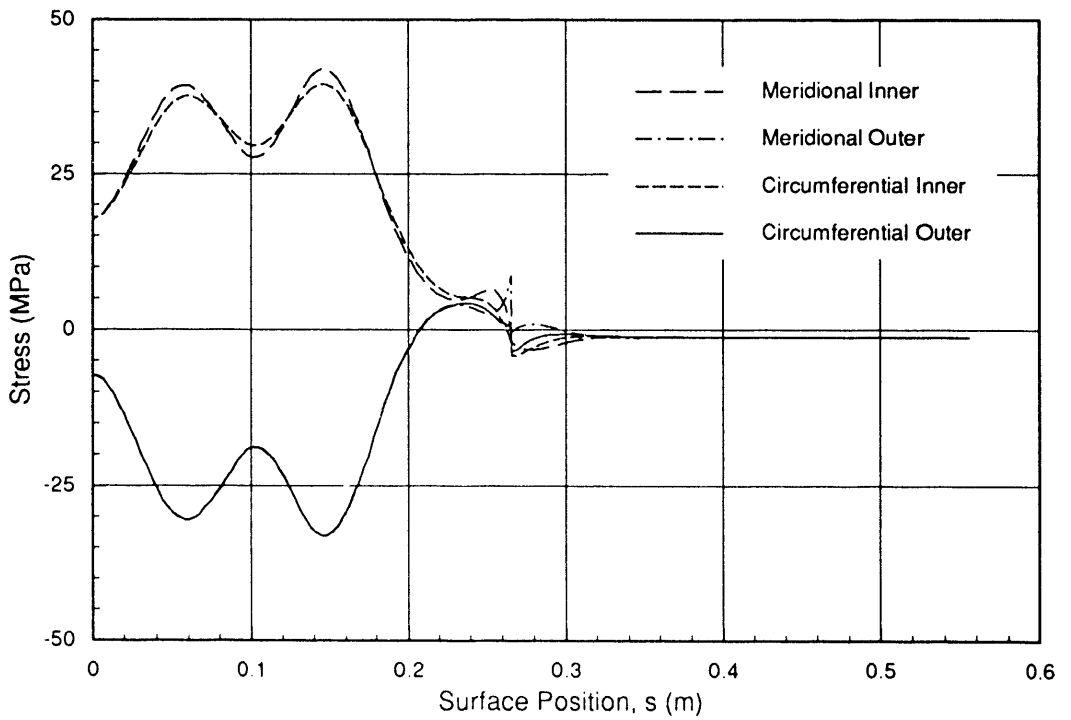

Figure 10. Receiver meridional and circumferential stress profiles during steady state operation (Step 7) for 316L SS.

The meridional and circumferential stress profiles in the Haynes 230 receiver are shown in Figure 11 and Figure 12 for Steps 3 and 7, respectively. Again, the stress gradient through the shell thickness is caused by the thermal gradient and is characteristic of a pure bending load. The stresses on the *inner* surface are tensile and the stresses on the *outer* surface are compressive. As in the 316L SS receiver, large stress gradients occur near the weld location due to the difference between the average temperatures of the absorber and aft dome. During startup, the maximum tensile stress is near 100 MPa while the maximum compressive stress is -77 MPa. During steady state operation, the *inner* surface values reach a maximum of 45 MPa and the *outer* surface stresses reach a maximum near -35 MPa. The stress near the absorber edge reduced to 20 MPa from a startup value of 90 MPa because the surface temperature of the aft dome and absorber is uniform during steady state operation. The small stress gradient present during steady state operation is due primarily to the geometric discontinuity of the seam-weld and the different thicknesses of the absorber and aft dome. The stress profile contains the double hump shape characteristic of the incident solar flux distribution shown in Figure 6. The maximum effective stress in the receiver is about 39 percent of the 260 MPa yield strength of Haynes 230 at 800 °C.

3.2.3 Conclusions on Material Selection

The temperature distributions obtained for 316L SS and Haynes 230 are essentially the same due to their similar material properties. The stresses in the 316L SS receiver are near the yield strength (103 MPa), while the higher yield strength of Haynes 230 results in maximum stresses about 39 percent of yield (260 MPa). The maximum stresses in both materials are generated during startup due to the uneven temperature distribution across the receiver surface. It should be noted that the larger stresses at the weld location during startup might not represent the actual operating stress because of the low resolution of the temperature data and the linear interpolation scheme applied to them. The stress magnitude would be smaller if startup temperatures across the receiver surface were more uniform.

3.3 Aft Dome Optimization

In the preceding calculations, a large stress jump was observed at the seam-weld interface of the absorber and aft dome. This jump could be attributed to two factors: the uneven temperature distribution over the receiver and the geometric discontinuity of the shell thicknesses at this location. The latter cause could be eliminated by reducing the aft dome shell thickness to one closer to the absorber. However, this would also increase the membrane stresses on the aft dome since the stress area would be reduced. The following calculations investigate the effect of reducing the aft dome thickness on the overall stress state of the receiver.

The reduced aft dome calculations utilize the same model and boundary conditions used for material assessment. Subsequently, the temperature profiles in the receiver were identical to

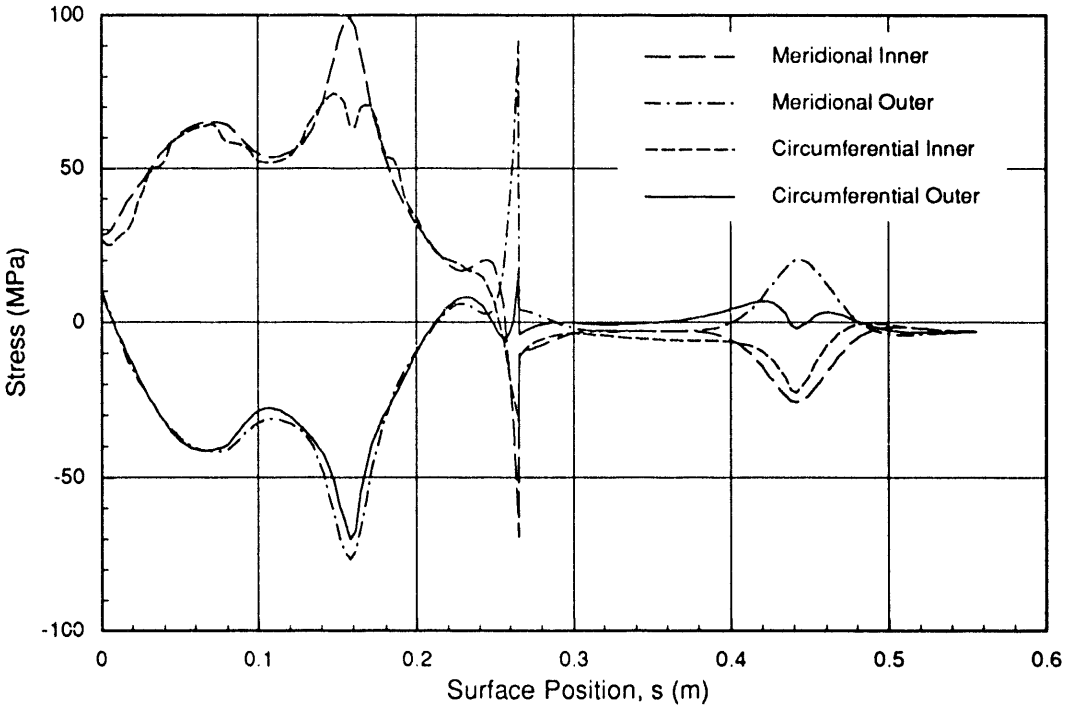

Figure 11. Receiver meridional and circumferential stress profiles during Step 3 of the receiver startup for Haynes 230.

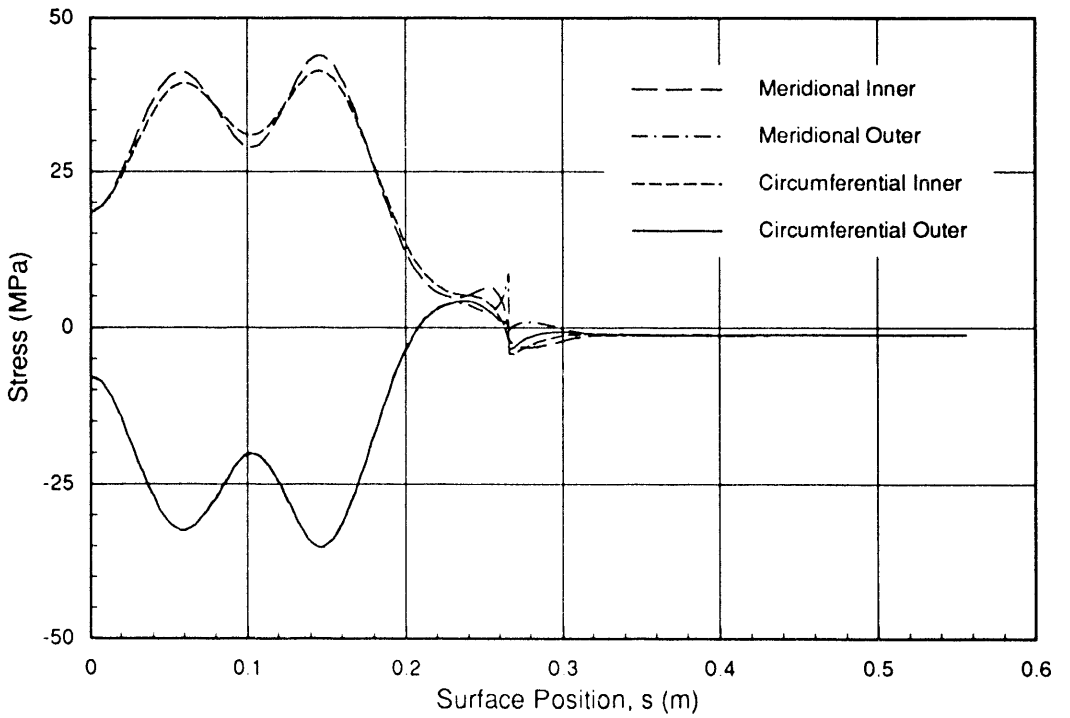

Figure 12. Receiver meridional and circumferential stress profiles during steady state operation (Step 7) for Haynes 230.

those shown in Figure 7 and Figure 8. Since these calculations were performed for optimization of the next-generation receiver, only Haynes 230 properties were considered. The calculations were performed for half-thickness (1.59 mm) and quarter-thickness (0.819 mm) aft domes. Again, the stress distributions are presented for Steps 3 and 7 for each calculation.

3.3.1 Half-Thickness Aft Dome

The meridional and circumferential stress profiles in the Haynes 230 receiver with a 1.59 mm aft dome are shown in Figure 13 and Figure 14 for Steps 3 and 7, respectively. Comparing the startup stress profiles of the full-thickness (Figure 11) and half-thickness (Figure 13) receivers shows that the maximum stress in the *inner* surface of the absorber reduces from 100 MPa for the full-thickness aft dome to 75 MPa for the half-thickness aft dome. Similarly, the maximum stress in the *outer* surface of the absorber reduces from -75 MPa for the full-thickness aft dome to -52 MPa for the half-thickness aft dome. The maximum stresses in the aft dome are also reduced for the half-thickness aft dome. These stress reductions are offset by a larger compressive membrane stress in the aft dome. A comparison of the steady state stress profiles of the full-thickness (Figure 12) and half-thickness (Figure 14) receivers shows that no significant changes occur. With the reduction in the aft dome thickness to 1.59 mm, the maximum effective stress in the receiver is below 29 percent of the yield strength, compared to 39 percent for the 3.18 mm aft dome.

3.3.2 Quarter-Thickness Aft Dome

The previous section showed that the stress state in the Haynes 230 receiver was improved by reducing the aft dome thickness to 1.59 mm. To determine if further stress reductions could be achieved, the Haynes 230 shell model was analyzed for equal absorber and aft dome thicknesses (0.819 mm). The meridional and circumferential stress profiles in the Haynes 230 receiver with a quarter-thickness aft dome are shown in Figure 15 and Figure 16 for Steps 3 and 7, respectively. Comparison of the startup stress profiles for the quarter-thickness (Figure 15) and half-thickness (Figure 13) aft domes shows that no appreciable changes occur with this additional reduction in aft dome thickness. The compressive membrane stress in the aft dome increased slightly. More significantly, the maximum stress near the weld reduced to 45 MPa from 75 MPa for the 1.59 mm-thick aft dome. This supports the original contention that the stress gradient near the seam-weld could be attributed to, among other things, the differential wall thickness of the absorber and aft dome. The steady state stress profiles (Figure 14 and Figure 16) show little change with further reductions in aft dome thickness.

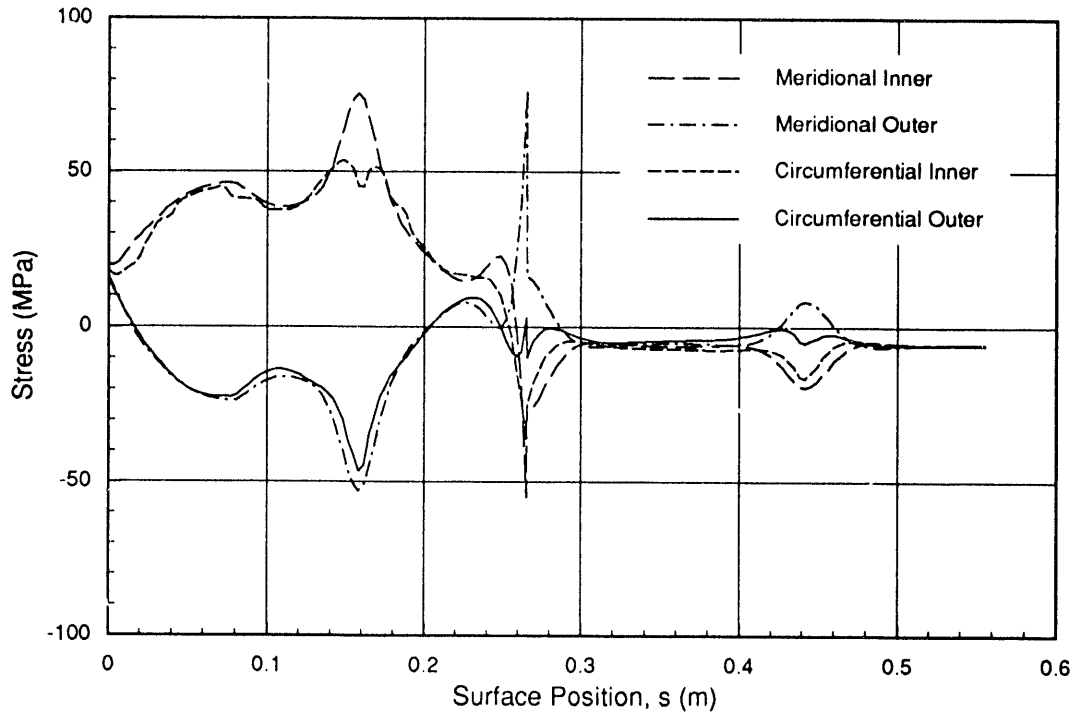

Figure 13. Receiver meridional and circumferential stress profiles during Step 3 of the receiver startup for Haynes 230 and a half-thickness (1.59 mm) aft dome.

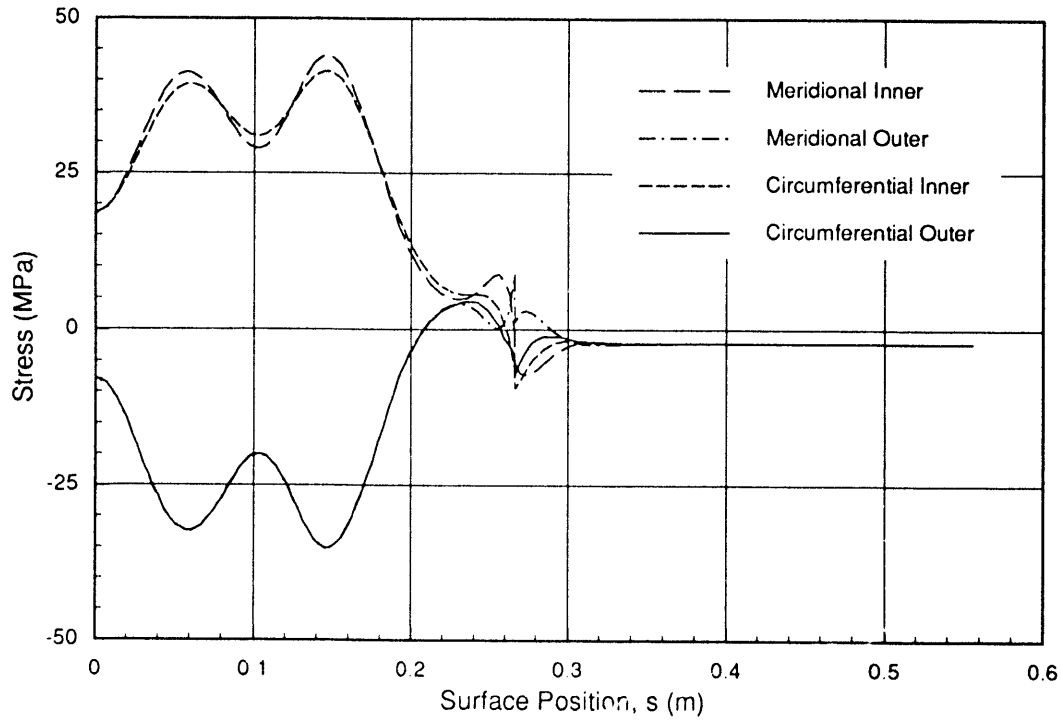

Figure 14. Receiver meridional and circumferential stress profiles during steady state (Step 7) operation for Haynes 230 and a half-thickness (1.59 mm) aft dome.

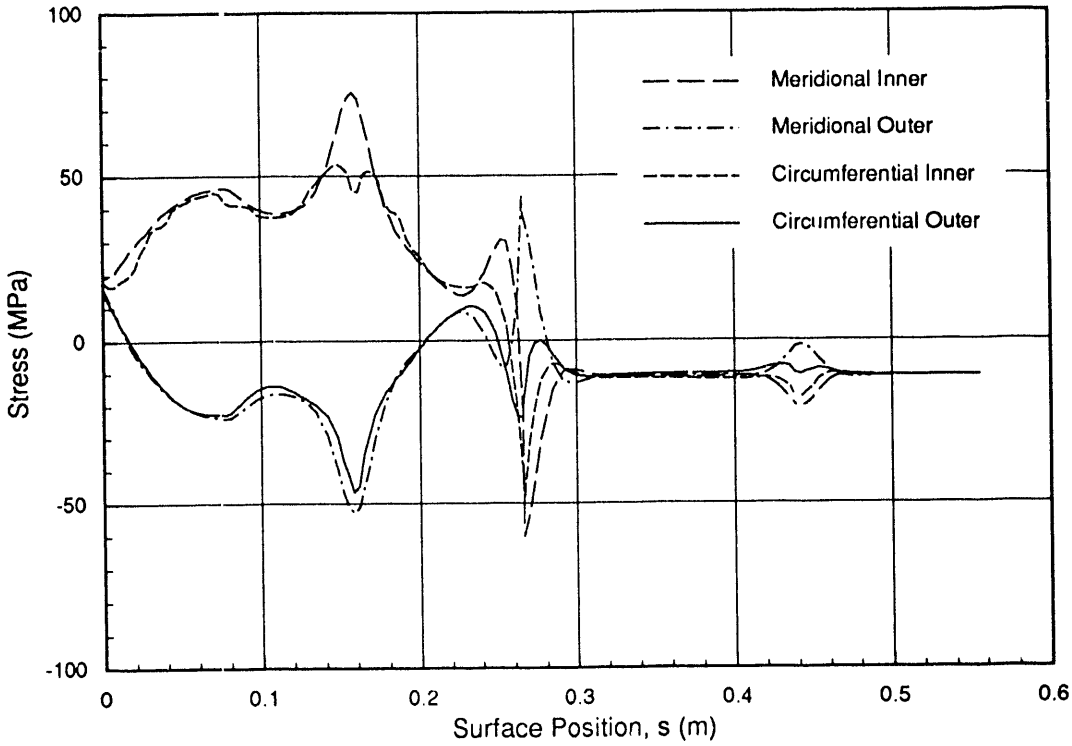

Figure 15. Receiver meridional and circumferential stress profiles during Step 3 of the receiver startup for Haynes 230 and a quarter-thickness (0.813 mm) aft dome.

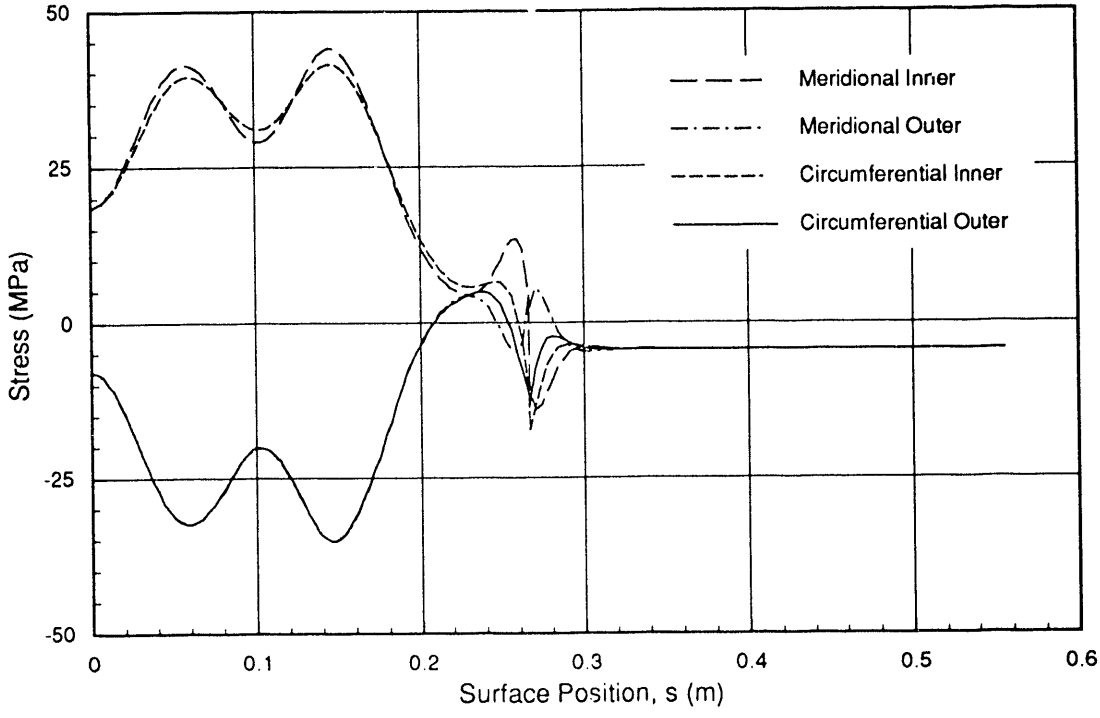

Figure 16. Receiver meridional and circumferential stress profiles during steady state operation for Haynes 230 and a quarter-thickness (0.813 mm) aft dome.

3.3.3 Optimum Aft Dome Thickness

The preceding calculations have demonstrated that a reduction in the aft dome thickness reduces the maximum absorber stresses during startup. Reducing the aft dome thickness from 3.18 to 1.59 mm resulted in a 25 percent decrease in absorber stress during startup. Although subsequent reductions in the aft dome thickness can further decrease absorber stress, there are diminishing returns as the absorber wall thickness is approached. The most significant benefit in reducing the aft dome thickness to 0.819 mm is a 40 percent reduction of the peak seam-weld stress. As expected, due to a substantial reduction in the stress area, the compressive membrane stress in the aft dome increased with reductions in aft dome thickness. Finally, reducing the aft dome thickness did not significantly affect the steady state stress profiles. It should be noted that these calculations do not consider the support load imposed on the aft dome by the 0.203-m-diameter pipe. These loads could place a limit on the aft dome thickness. A three-dimensional analysis of the receiver would be required to investigate gravity loading.

4 Seam-Weld Fatigue Analyses

As the development of a next-generation receiver progressed, the program focused on optimization and life issues. The proposed seam-weld crevice between absorber and aft dome was identified as a potential threat to the projected lifetime of the receiver [9]. Inspection of the *inner* surface stress distributions as calculated in the shell analyses (Figure 11 and Figure 12) shows that the *inner* surface of the weld is in compression during both startup and steady state phases of operation, in both the circumferential and meridional components. Because the shell analyses cannot capture the detail of the seam-weld, a more detailed analysis of the weld was performed and is presented in this section.

Treating the weld crevice as a crack (i.e. neglecting crack initiation time), the stress distribution near the seam-weld was investigated for constant amplitude load fluctuation between the unloaded (off-sun) condition and steady state (on-sun) thermal loading. The worst case start up condition (Step 3) was not considered for reasons which will be discussed later. Based on linear elastic fracture mechanics (LEFM) techniques [12], the fluctuation in the stress intensity factor near the crack tip was calculated for one load cycle. These calculations were performed using the J-integral method and crack opening-displacement field equations.

The following section describes the finite element model used to study the seam-weld. Next, the fracture parameters used in these calculations are defined and briefly explained. Finally, a description is given of the cyclic loads applied to the receiver. Calculations are presented for the elastic load cycling between on-sun and off-sun conditions. Additional calculations are presented in which assumptions are made to approximate long-term creep effects. The results of the analyses are given for the various load cases representing the amplitude of the applied loads. These calculations are used in conjunction with fatigue data to determine whether a fracture will propagate through the seam-weld.

4.1 Finite Element Model

A cross section of a candidate seam-weld between the absorber and aft dome is shown in Figure 17. All of the candidates under consideration have in common the built-in "crack" that is evident in this photograph. To capture the detail of the seam-weld, a mesh was needed with more detail than the shell model used in the previous analyses. The finite element mesh of the reflux pool-boiler receiver is shown in Figure 18. The model consists of 1757 axisymmetric continuum elements and 6986 nodes. The elements are 8-node quadrilaterals written for fully coupled temperature-displacement analysis. These elements use biquadratic displacement interpolation and bilinear temperature interpolation. Because the elements are higher order in displacement and the stresses are linear, only two elements were used through the thickness of the absorber and aft dome at locations away from the seam-weld. As is recommended in fracture mechanics analysis, the mesh is focused at the tips of the weld notches. In addition, the mid-side nodes of the elements closest to the notch tip are moved to the 1/4-point positions next to the crack tip

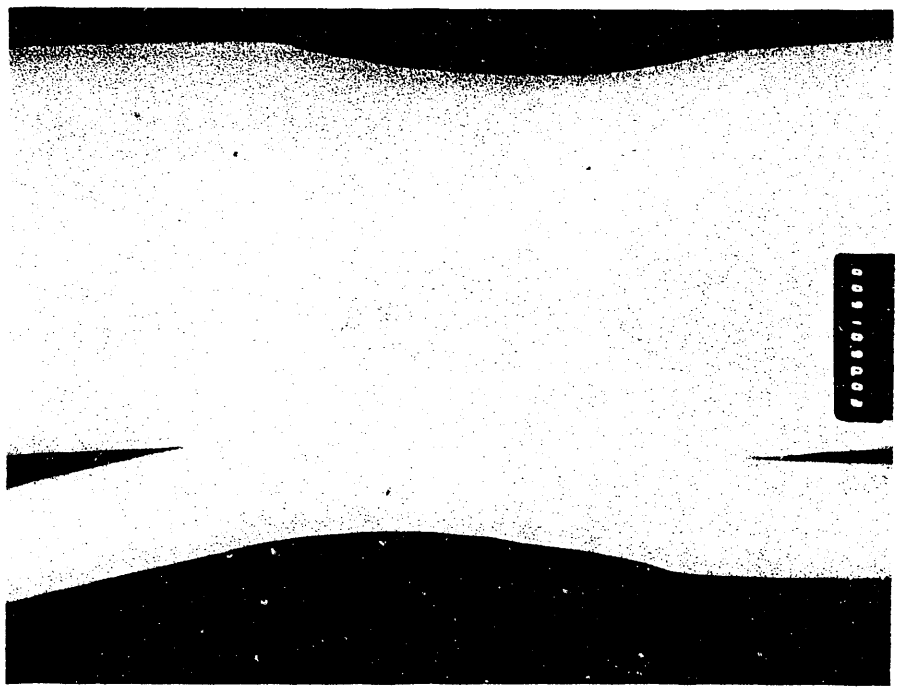

Figure 17. Cross section of a candidate seam-weld joining the absorber and aft dome of the reflux pool-boiler receiver.

as illustrated in Figure 19. Coincident nodes at the crack tip are constrained to have the same displacements. These adjustments produce a $r^{-1/2}$ strain singularity near the notch, where r is the radial distance from the notch tip. Based on the previous shell element calculations, the upper notch was expected to be subjected to a slightly harsher stress environment at steady state operating conditions than the lower notch. However, both notch meshes were concentrated so that the stress intensification could be investigated at each side of the weld.

4.2 Definition of Fatigue Crack Growth Parameters

Linear elastic fracture mechanics (LEFM) relates the stress magnitude and distribution in the vicinity of a crack tip to the nominal stress in the vicinity of the crack; the size, shape and orientation of the crack; and the material properties [12]. The magnitude of the elastic-stress field for opening mode displacement (Mode I) can be described by a single parameter, K_I, designated the stress intensity factor. Unstable fracture may occur when the stress intensity at the crack tip (K_I) reaches the *critical stress intensity factor*, K_c. The critical stress intensity factor represents the ability of a material to withstand a given crack tip stress intensity and resist progressive crack extension.

The stress intensity factor is related to the nominal stress σ and flaw size a for a given material as follows:

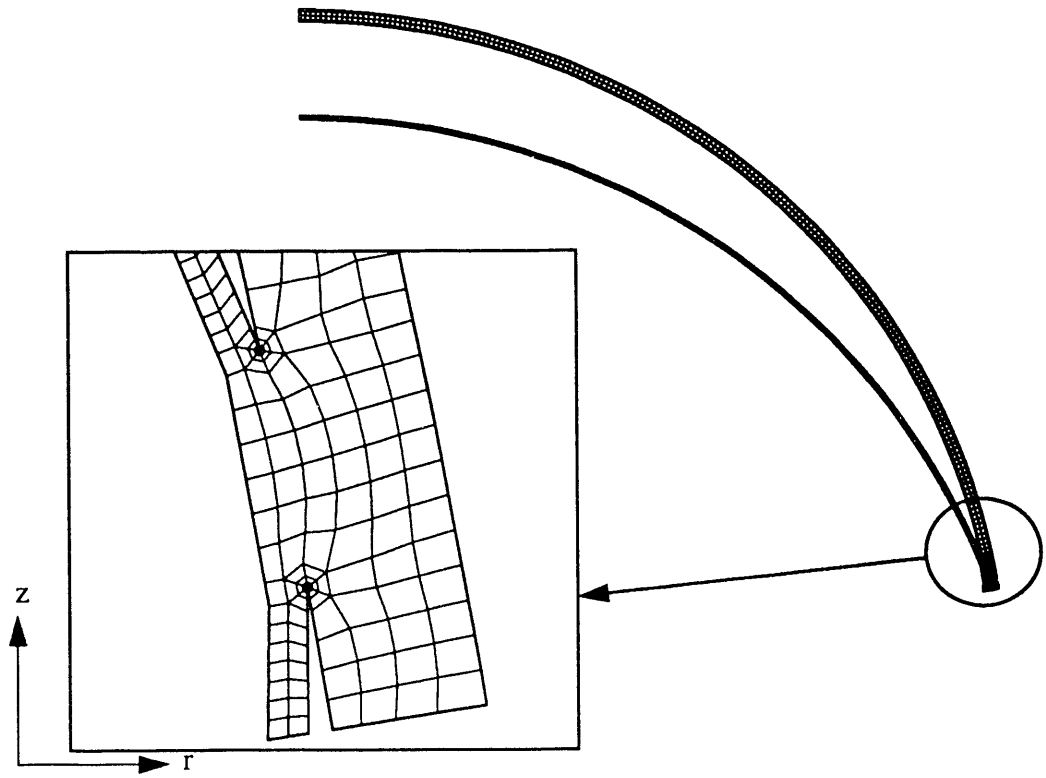

Figure 18. Finite element mesh of the reflux pool-boiler receiver.

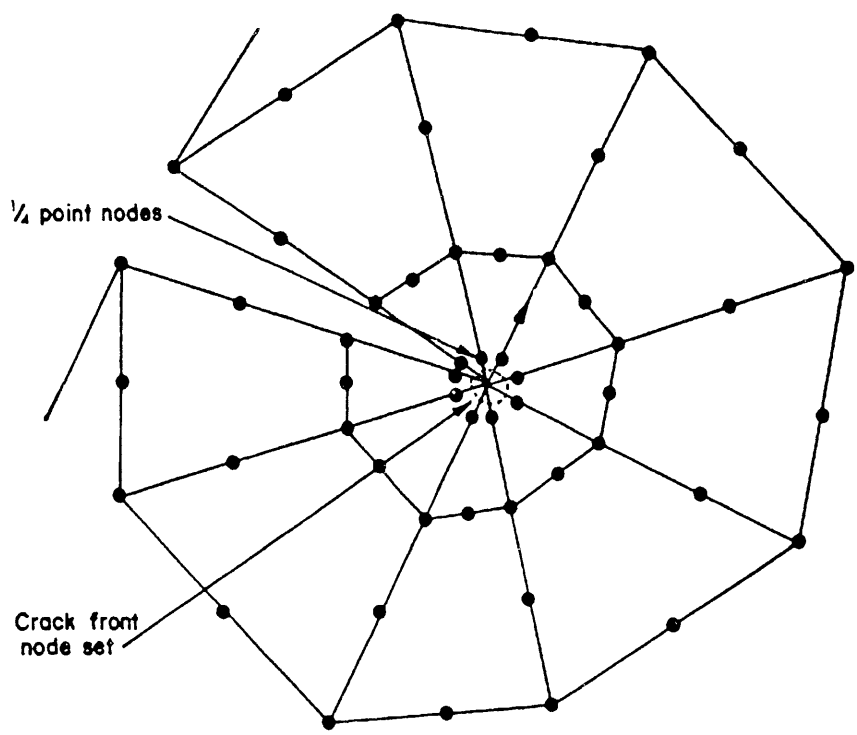

Figure 19. Focused mesh used at seam-weld notches [7].

$$K_I = C\sigma\sqrt{a} \tag{2}$$

where the constant C is a function of the crack geometry. If a particular combination of crack size and stress in a structure (K_I) reaches the K_c level, fracture can occur.

Subcritical or fatigue crack growth may also occur where the load conditions are such that the stress intensity factor K_I is significantly less than K_c. Under constant amplitude load fluctuation, the subcritical crack growth rate can be estimated from a knowledge of the fluctuation of the stress intensity factor, ΔK_I. The most common presentation of crack growth data is a log-log plot of the crack growth per cycle, da/dN, versus the fluctuation of the stress intensity factor, ΔK_I. Figure 20 illustrates the form of typical fatigue-crack growth data. The propagation behavior for metals can be divided into three regions. In Region I the data is characterized by near-threshold behavior. In this region, a small decrease in the stress intensity factor results in a large decrease in the crack growth rate (da/dN). Below this "fatigue-threshold" cyclic stress intensity factor, ΔK_{th}, a crack will not propagate under cyclic stress. For most steels, this threshold is approximately 6 $MNm^{-3/2}$ (5.5 $ksi\sqrt{in}$) [12]. In Region II the data exhibits fatigue-crack propagation behavior which can be mathematically modeled as

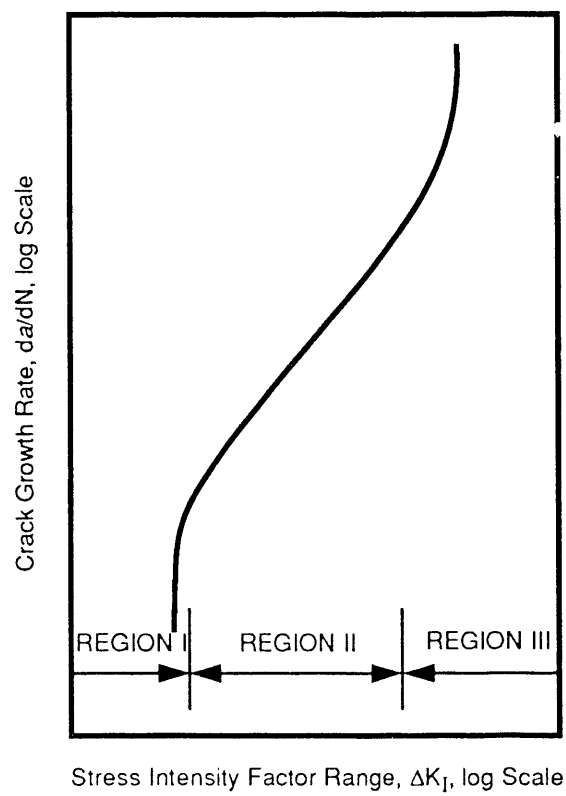

Figure 20. Schematic representation of fatigue-crack growth data [12]

$$\frac{da}{dN} = A\,(\Delta K_I)^n \tag{3}$$

where A and n are constants. In Region III the fatigue crack growth rate increases rapidly with small changes in ΔK_I.

In the present calculations, the stress intensity factor is calculated using the J-integral method and crack opening-displacement field equations. Both methods are based on either plane strain or plane stress assumptions. For the following axisymmetric analyses, the plane strain assumption was used because the corresponding equations yield a conservative approximation of the stress intensity factor. A review of the two methods used to calculate the stress intensity factor is presented next. More information on the subject can be found in references [12, 13, 14].

4.2.1 J-Integral

The J-integral is a path-independent line integral about the crack tip which is a measure of the stress-strain field ahead of the crack. The line integral, J, is defined for either elastic or elastic-plastic behavior as follows:

$$J = \int_R W\,dx_2 - T\left(\frac{\partial u}{\partial x_1}\right) ds \tag{4}$$

where R is any contour surrounding the crack tip as shown in Figure 21, W is the strain energy density $\int_0^\varepsilon \sigma d\varepsilon$, T is the traction vector defined according to the outward normal n along R, u is the displacement vector, and ds is the arc length along contour R. The J-integral may be interpreted for elastic materials as the rate of change in potential energy between two identically

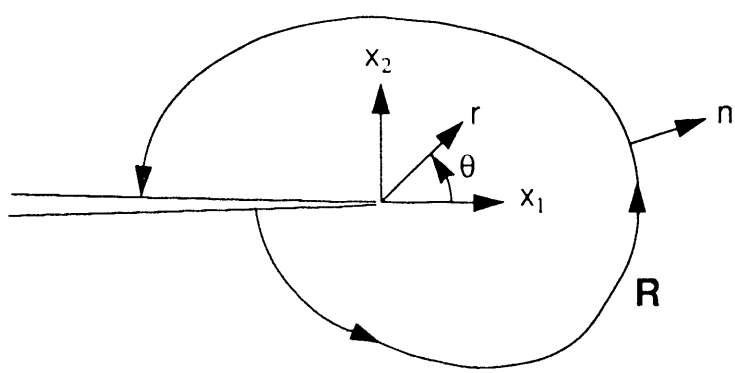

Figure 21. Crack-tip region, coordinate system and path independent J-integral.

loaded bodies having slightly different crack lengths. For elastic plane strain conditions, the stress intensity factor is related to the J-integral parameter as follows:

$$K_I = \sqrt{\frac{J_I E}{(1-\nu^2)}} \tag{5}$$

ABAQUS contains a procedure for calculating the J-integral based on the method of virtual crack extension [14]. The evaluation of the line integral may be thought of as a contour line passing through a ring of elements surrounding the crack front. The evaluation can be performed for a number of such rings of elements. Since the integral is path independent, these values should be the same. For the particular mesh used in the present calculations, a J-integral calculation is performed for each of the three rings surrounding each crack tip (see Figure 18). Thermally loaded problems present a difficulty since the potential used in the formulation of the J-integral procedure is structural only. This problem is addressed in Section 4.2.3.

4.2.2 Crack Opening-Displacement Equations

The crack opening-displacement field equations describe the stress and displacement fields in the vicinity of a crack in terms of the stress intensity factor, K_I, and other material properties. The Mode I displacement field equations are:

$$\begin{pmatrix} u_1 \\ u_2 \end{pmatrix} = \frac{K_I}{2\mu}\left(\frac{r}{2\pi}\right)^{1/2} \begin{pmatrix} \cos(\theta/2)\,[\kappa - 1 + 2\sin^2(\theta/2)] \\ \sin(\theta/2)\,[\kappa - 1 + 2\cos^2(\theta/2)] \end{pmatrix} \tag{6}$$

where μ is the shear modulus, r is the radial distance from the crack, and θ is the orientation of the point as shown in Figure 21. For plane strain conditions $\kappa = 3 - 4\nu$. These equations can be found in any fracture mechanics text [12, 13]. In the present calculations, the stress intensity factor was calculated from the nodal displacements for the nodes along the interior surface of the weld notch (θ=180°). For this case, u_1=0 and u_2 reduces to

$$u_2 = \frac{K_I}{2\mu}\left(\frac{r}{2\pi}\right)^{1/2} (\kappa - 1) \tag{7}$$

Using the finite element analysis results, the opening mode displacements (u_2) for the first six nodes on each side of the notch were calculated relative to the displacement of the crack tip. Using Equation (7), the stress intensity factor of the weld notch was calculated from the relative displacements. As in the case of the J-integral method, the equations which describe the displacement field at a crack tip consider structural loading only.

4.2.3 Application to Thermally Loaded Problems

Because typical methods of calculating K_I do not include thermal loads in their formulation, they cannot be blindly applied to coupled thermal-structural analyses. For thermal problems, ABAQUS recommends that very small elements be used near the crack tip such that the thermal load is treated simply as a body force [14]. This method was used for the coupled thermal-displacement analyses of the reflux pool-boiler receiver. In addition, calculations were performed with only the structural loads applied. The results were compared to the thermally loaded problems to investigate the effects of thermal strains on the local stresses at the crack tip.

4.3 Cyclic Load Environment

The reflux pool-boiler receiver is subjected to constant amplitude load fluctuation between off-sun and on-sun conditions. Early in the life of the receiver, the on-sun loads result from the thermal and structural loads at steady state operating conditions, and the off-sun loads are due only to the vacuum that exists in the receiver. After a long period of operation, the on-sun deviatoric stresses will relax due to high-temperature creep. When the receiver is cooled to off-sun temperatures, a residual stress state will exist in the receiver. In this study, the off-sun residual stresses are approximated by reversing the thermal loads on the receiver. This was accomplished by simply reversing the sign of the coefficient of thermal expansion.

The reversed thermal load approximation assumes the receiver is stress-free when on-sun. This assumes the initial on-sun stresses have no volumetric component, because only deviatoric stresses produce creep. Since the meridional and circumferential components are nearly equal and the radial component is zero, there is a nonzero volumetric stress component. As a result, the on-sun stresses will not relax to zero and the reversed thermal load approximation yields conservative results.

Four load cases were analyzed using the reflux pool-boiler receiver model: (1) on-sun structural loading (Equation 1 for on-sun temperatures) with thermal loading (flux), (2) on-sun structural loading with no thermal loads, (3) off-sun structural loading (Equation 1 for off-sun temperatures) with reversed on-sun thermal loads, and (4) off-sun structural loading with no thermal loads. The first case represents the steady state operating conditions of the on-sun receiver. The third case, as previously stated, represents an approximation of the off-sun residual stress state when the receiver is held at on-sun temperatures for a long period of time and is then cooled to room temperature. The calculations with no thermal load were performed to determine the contribution of thermal strains to the stress state near the crack tip.

The fracture parameters calculated for the above four cases were used to calculate ΔK_I for the two cyclic load environments: (1) at early receiver life, and (2) after relaxation of on-sun stresses. Early in the receiver life, the stress fluctuation at the notch tip results from load cycling between thermal loading (Case 1) and off-sun loads due to internal pressure (Case 4). For the

stress relaxation approximation, the stress fluctuation results from cycling between the reversed thermal loading (Case 3) and the on-sun "stress-free" condition.

4.4 Analysis Results for Steady State Operation

In the following sections the results of the four load cases are presented. First, the stress distributions near the weld crevice are investigated. The results of the calculations are presented in terms of the largest principal stress in the vicinity of the upper seam-weld notch since it is exposed to the harshest stress environment of the two weld notches. Post-processing of the calculations was performed using BLOT [15] which displays an 8-node quadrilateral as four 4-node quadrilaterals. Consequently, plots of the results appear to have greater mesh refinement than the model shown in Figure 18. In the last sub section, the results from the fracture parameter calculations are presented.

4.4.1 Case 1: On-Sun Structural and Thermal Loading

For verification of the finite element model, the results of this load case were compared to the results of the corresponding analysis performed using shell elements. The nodal temperatures computed along the *outer* surface of the absorber are shown in Figure 22 compared to the shell calculations. The temperatures from the two analyses are essentially identical. The stress output variable which is common to both analyses is the circumferential stress. Figure 23 compares the circumferential stress in the *outer* and *inner* surfaces of the absorber for both analyses. As in the shell calculations, the results show a stress gradient in the absorber wall which is caused by the thermal gradient through the wall. This stress distribution is characteristic of pure bending, with tensile stresses on the *inner* surface and compressive stresses on the *outer* surface. The results for the 8-node quadrilateral calculations are lower then the shell calculations because the stresses in the 8-node quadrilaterals are evaluated at the quadrature points of the elements, not at the surface. Hand calculations, extrapolating the temperature to the surface, verify that the analysis results agree.

Figure 24 is a plot of the largest principal stress distribution near the upper weld notch. The white region at the tip of the notch represents stresses beyond the range of the contour plot. The plot shows that a compressive stress field exists in front of the notch. A compressive stress field is not conducive to crack propagation. Furthermore, the magnitude of the stress is low, with maximum compressive stresses near 12 MPa (1.74 ksi).

It is interesting to compare the continuum element results with the previous shell calculations under the same steady state load conditions. Note that the circumferential and meridional stress components in the corresponding shell analyses (Figure 12) are on the order of 7 MPa on the *inner* surface near the seam weld. This compares well with the results presented in this section.

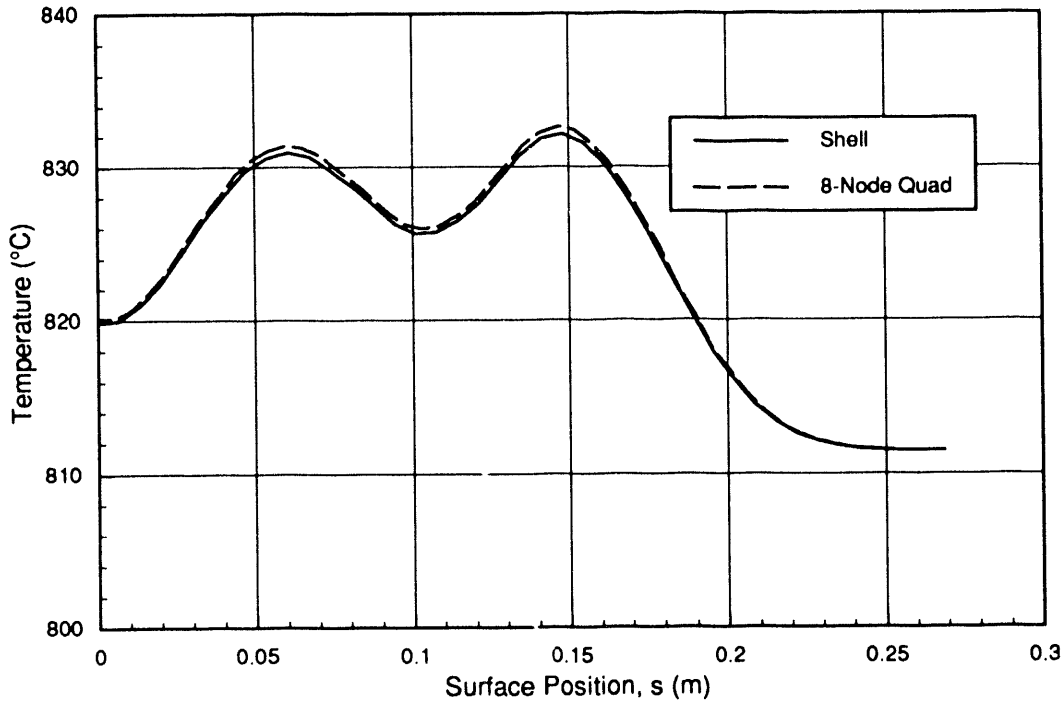

Figure 22. Temperature at the *outer* surface of the absorber calculated using axisymmetric shell elements and 8-node axisymmetric solid elements for on-sun structural and thermal loading (Case 1).

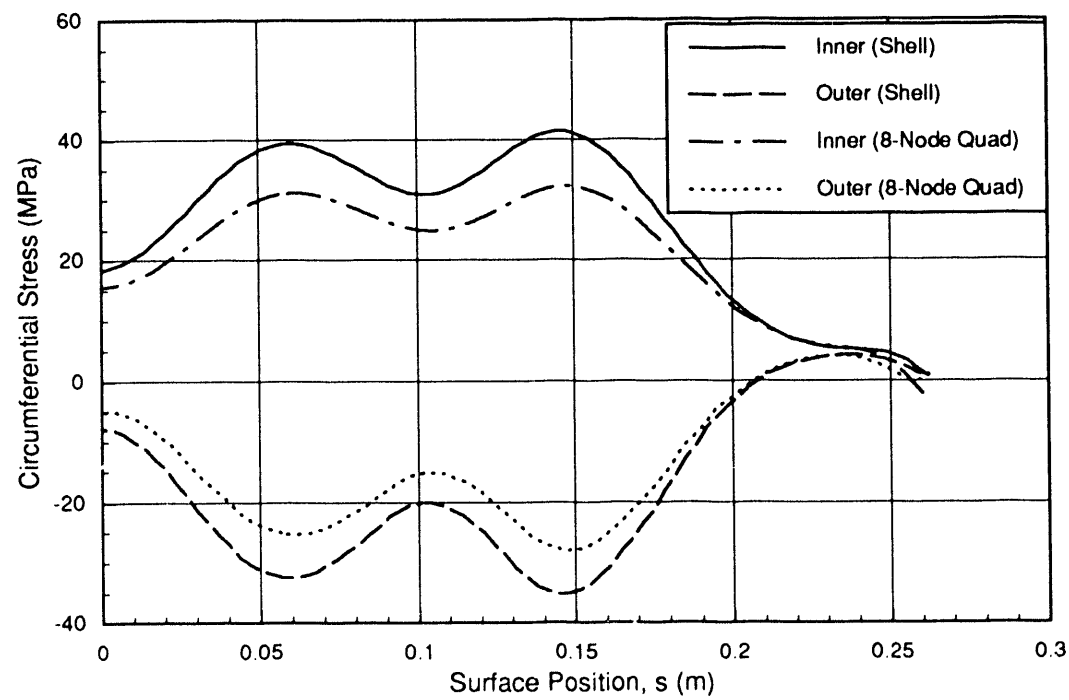

Figure 23. Circumferential stress in absorber calculated using axisymmetric shell elements and 8-node axisymmetric solid elements for on-sun structural and thermal loading (Case 1).

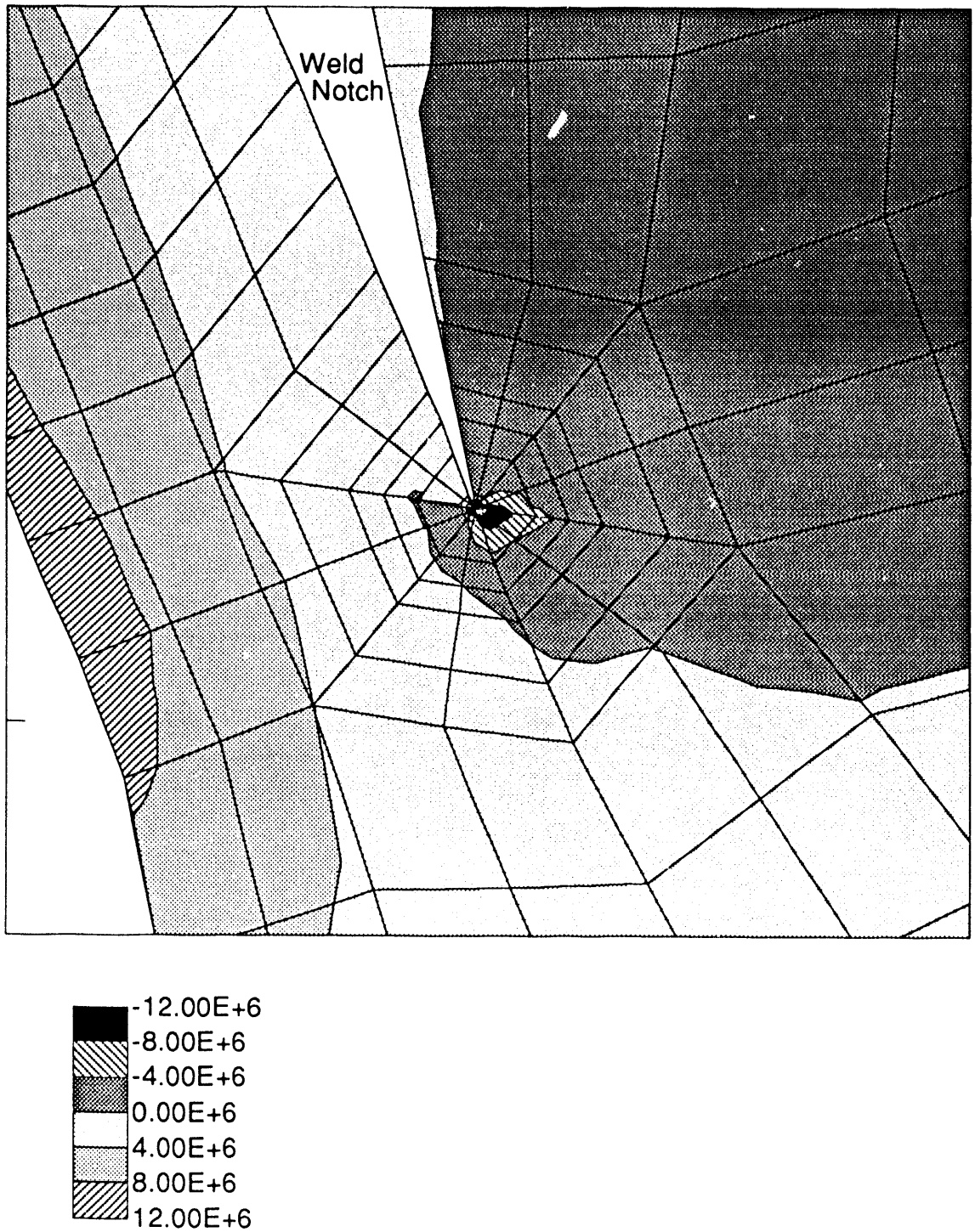

Figure 24. Largest principal stress near the weld discontinuity for the case of thermal loading and (P_{amb}-P_{int}) = 32.9 kPa (Case 1).

4.4.2 Case 2: On-Sun Structural Loading and No Thermal Loads

The compressive stress field observed in the previous analysis was expected because the absorber tries to expand more than the aft dome, producing a compressive loading at the seam-weld. To determine the contribution of the structural load to the stress distribution near the weld, the calculation was repeated with the thermal loads removed. Figure 25 is a plot of the circumferential stresses in the *inner* and *outer* absorber surfaces under these load conditions. When compared to Figure 23, these plots demonstrate that the thermal loads determine the overall stress profile in the receiver. The stress profile in Figure 23 is characterized by the distinctive double hump produced by the incident solar flux distribution shown in Figure 6. However, this double hump is not present in Figure 25. Note that the average of the *inner* and *outer* stresses, the membrane stress, in Figure 25 is nearly the same as that in Figure 23. This indicates that the structural loads generate the membrane stress, while the thermal loads produce a nearly pure bending stress.

The largest principal stresses near the weld notch is plotted in Figure 26 for the structurally loaded receiver with no thermal loads. These stress contours are nearly identical to those for Case 1, indicating that the localized stress distribution near the seam-weld depends more on the internal pressure of the receiver than on the thermal loads. Since the stress distribution ahead of the notch tip is the same with or without thermal loading, this suggests that thermal

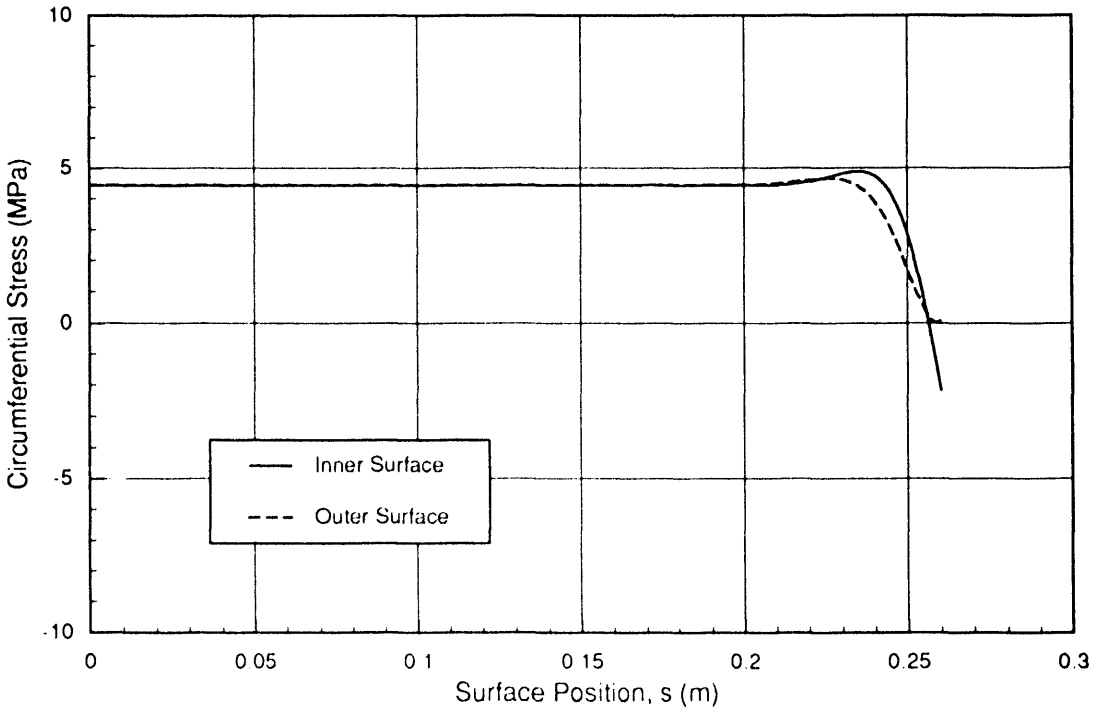

Figure 25. Circumferential stress in absorber for on-sun structural loading and no thermal loads (Case 2).

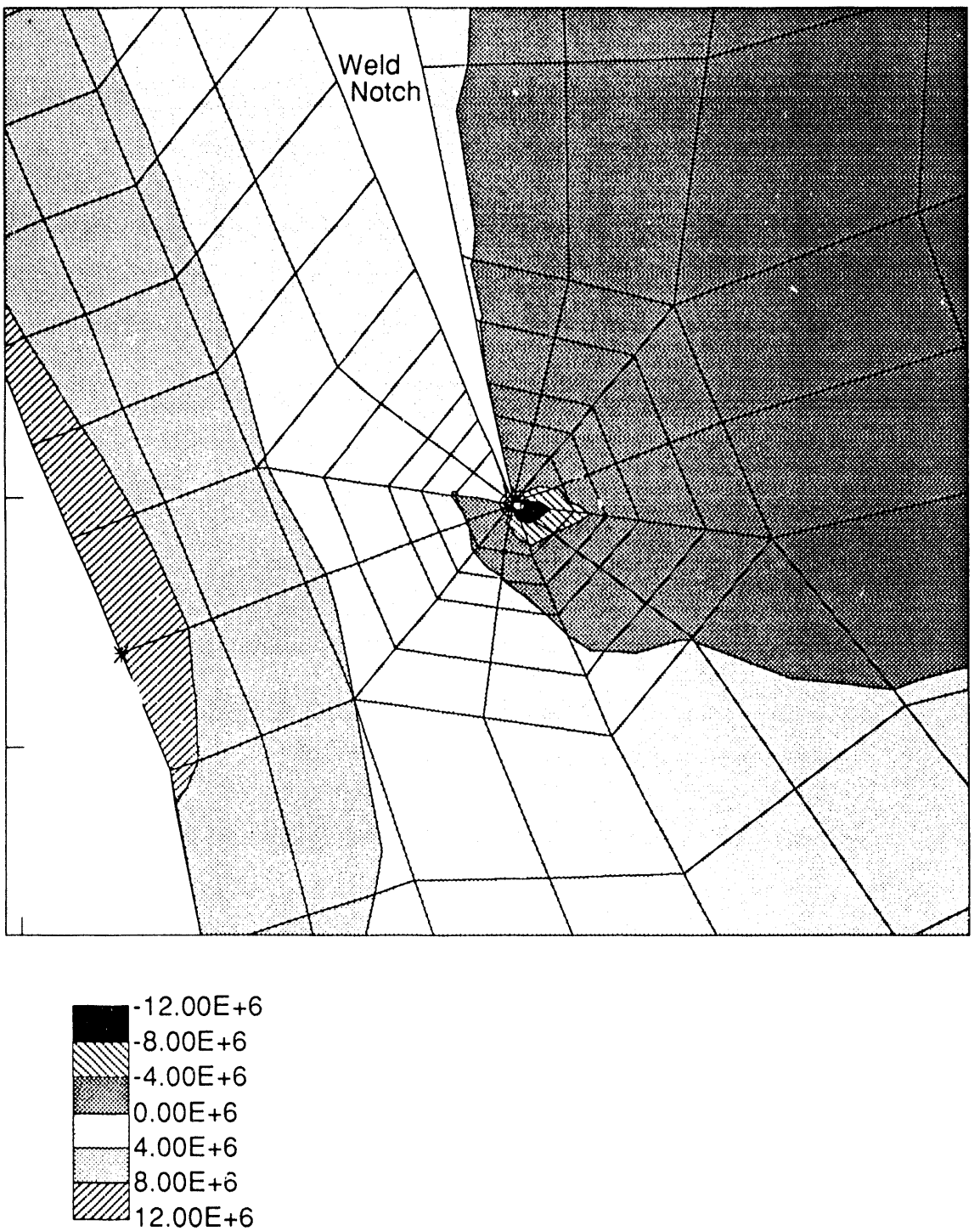

Figure 26. Largest principal stress near the weld discontinuity for the case of no thermal loading and (P_{amb}-P_{int}) = 32.9 kPa (Case 2).

loads need not be considered when calculating K_I.

4.4.3 Case 3: Off-Sun Structural Loading with Reversed On-Sun Thermal Loads

To reverse the thermal loads applied to the reflux pool-boiler receiver during steady state operation, the sign of the coefficient of thermal expansion was changed. The circumferential stress profile in the absorber with reversed thermal loads is shown in Figure 27 for comparison with Figure 23. The stress profiles are of similar magnitude, but opposite in sign. The *inner* surface is in compression, while the *outer* surface is in tension. Again, the plot is characterized by the distinctive double hump produced by the thermal flux distribution shown in Figure 6. This stress profile is an approximation to the off-sun residual stress state after the on-sun thermal stresses have relaxed. A plot of the largest principal stress near the seam-weld notch is shown in Figure 28. Again, the stress field is compressive in the seam-weld ahead of the notch. Crack propagation will not occur into a compressive stress field. Furthermore, the magnitude of the stress distribution near the seam-weld notch is small, with maximum stresses on the order of 24 MPa (3.48 ksi).

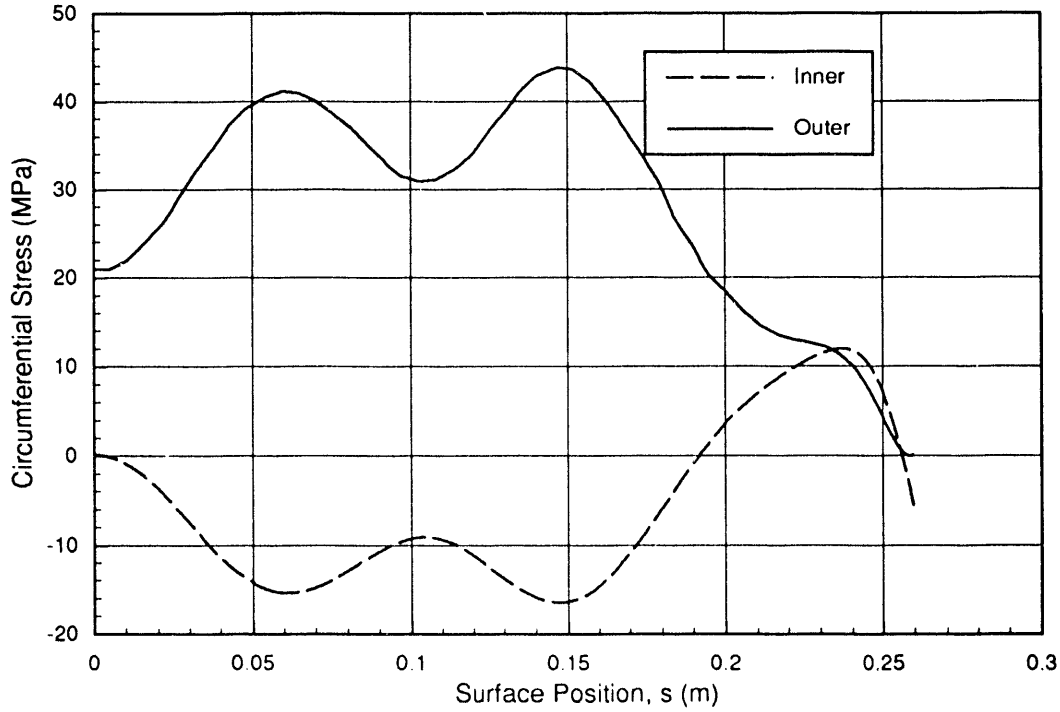

Figure 27. Circumferential stress in the absorber as a function of surface position for off-sun structural and reversed thermal loading (Case 3).

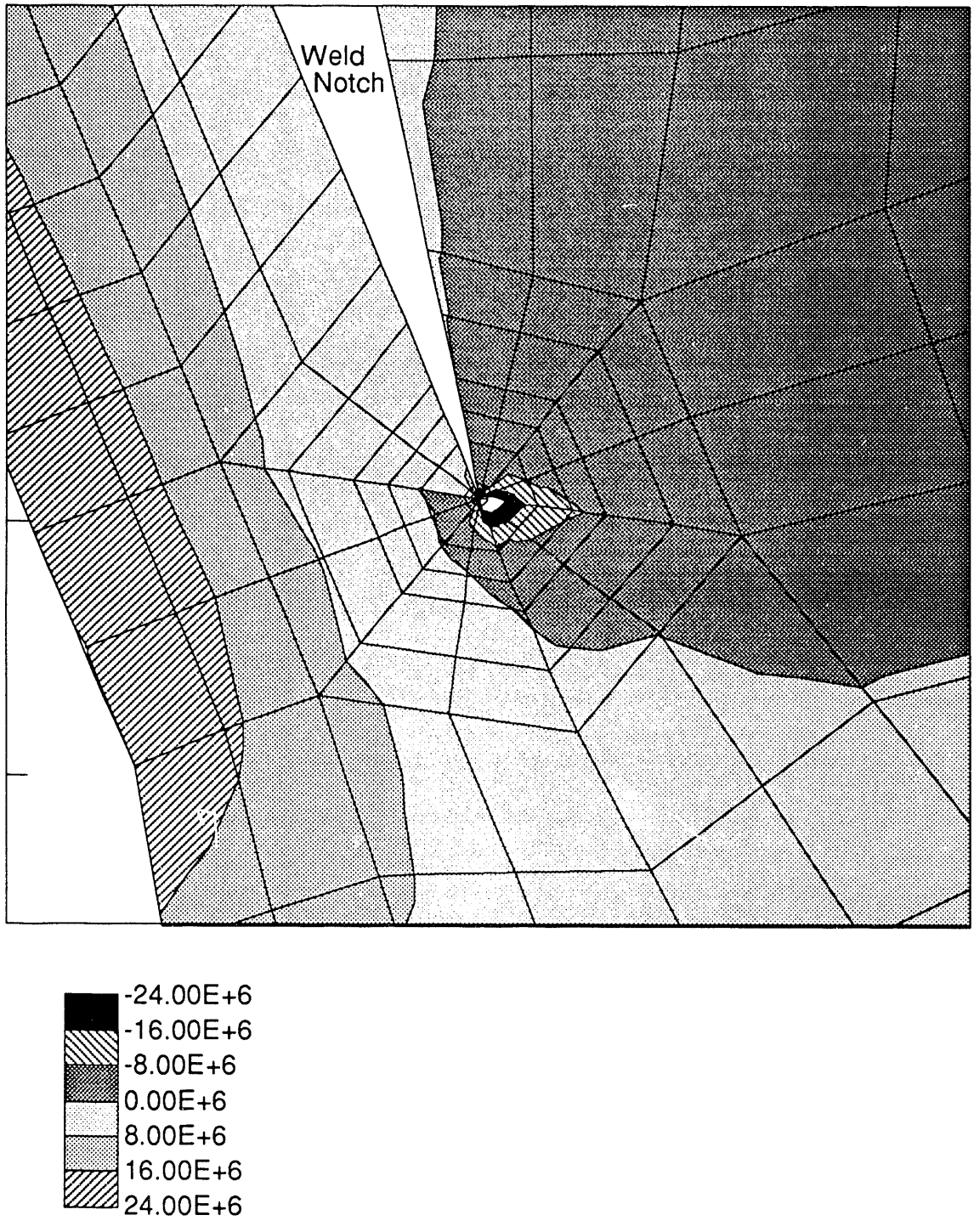

Figure 28. Largest principal stress near the weld discontinuity for the case of reversed thermal loading and (P_{amb}-P_{int}) = 84.1 kPa (Case 3).

4.4.4 Case 4: Off-Sun Structural Loading with No Thermal Loads

This particular load case was analyzed to determine (1) the contribution of thermal loading to the seam-weld stress distribution in the previous case and (2) the off-sun load that the receiver is subjected to prior to any stress relaxation. Figure 29 is a plot of the circumferential stress in the absorber for off-sun structural loading and no thermal loads. The average of the *inner* and *outer* stresses, the membrane stress, is approximately twice that of the receiver with on-sun structural loading and no thermal loads (see Figure 25). This is due to the higher internal pressure loads generated when the receiver is off-sun. Furthermore, the membrane stress for this load case is approximately the same as that in Figure 27, the case of off-sun structural loading with reversed thermal loads. This again indicates that the structural loads are dominant in determining the membrane stress in the receiver, while the thermal gradients produce nearly pure bending stresses.

The maximum principal stress distribution near the upper seam-weld notch for Case 4 load conditions, illustrated in Figure 30, is nearly identical to that of Case 3 (see Figure 28). This indicates that the stress distribution local to the upper seam-weld notch depends more on the structural loads, which induces a membrane stress, than the thermal loads, which induce pure bending. This again indicates that the stress intensity factor can be calculated neglecting thermal loads.

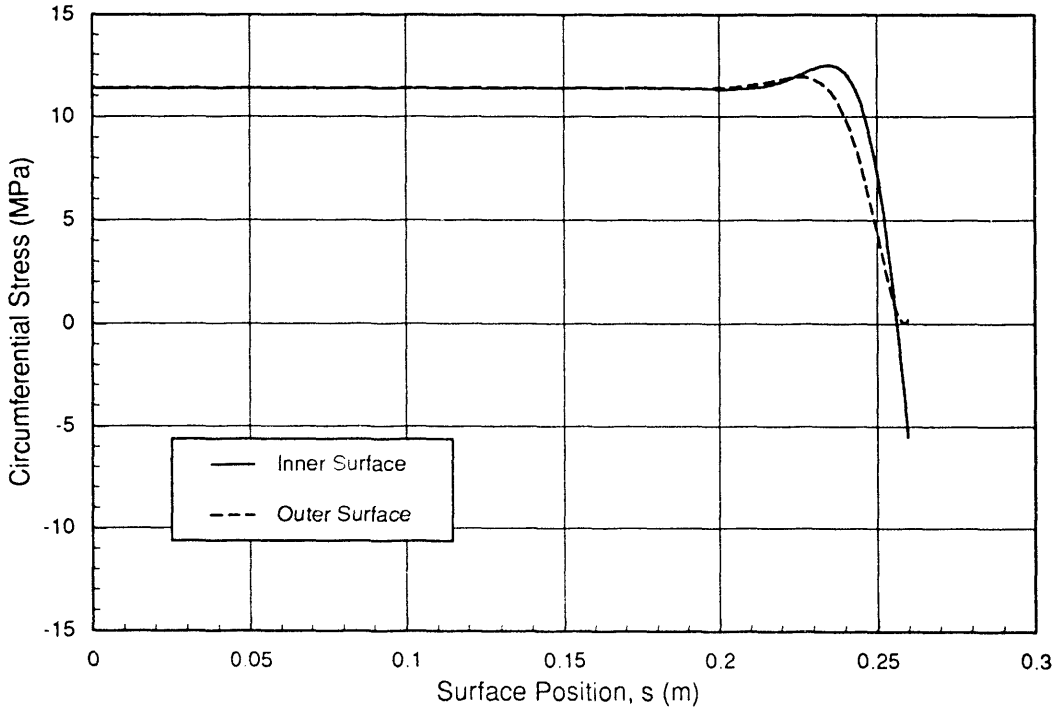

Figure 29. Circumferential stress in the absorber as a function of surface position for the case of off-sun structural loading and no thermal loads (Case 4).

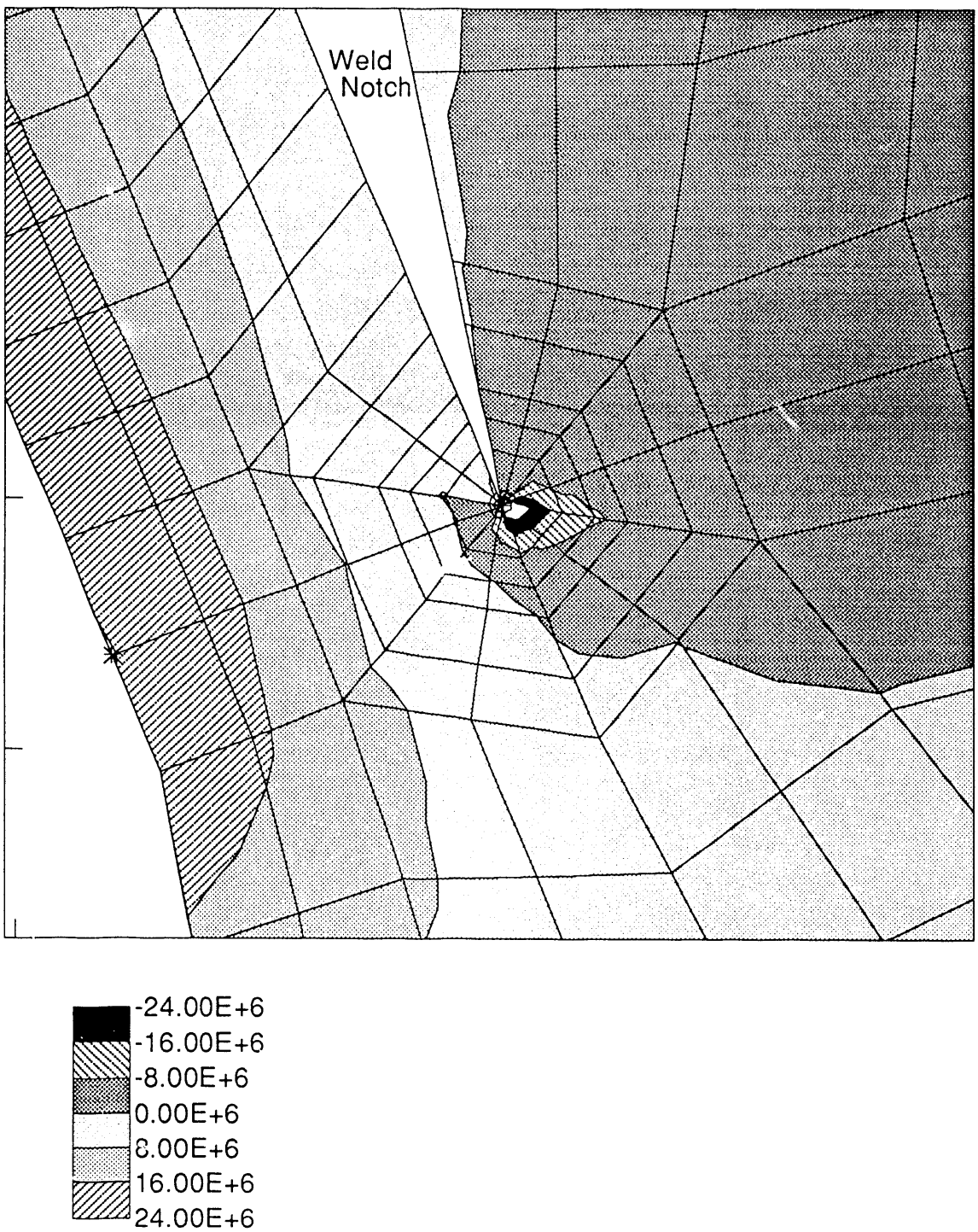

Figure 30. Largest principal stress near the weld discontinuity for the case of no thermal loading and (P_{amb}-P_{int}) = 84.1 kPa (Case 4).

4.4.5 Fluctuation of Stress Intensity Factor

In all four of the cases presented above the stress intensity factor, K_I, was calculated using the J-integral feature in ABAQUS as well as the opening-displacement field equations. Based on inspection of the stress field ahead of the notch in the previous sections, it was concluded that the thermal loads should not contribute significantly to K_I. Thus, any differences in K_I contributed by the thermal load could be attributed to free thermal expansion of the receiver. In all cases, these methods yielded K_I values on the order of 0.05 to 0.40 $MNm^{3/2}$ (0.046 to 0.367 $ksi\sqrt{in}$) for the upper seam-weld notch. The smaller values of K_I were obtained for 0.5 atm applied pressure, and the larger for the 1 atm applied pressure. The best correlation between the J-integral and crack opening methods was obtained for the cases with no thermal loads. As expected, the same parameters were orders of magnitude smaller at the lower seam-weld notch. Based on these calculations, the fluctuation of the stress intensity factor in both seam-weld notches is considerably lower than the fatigue-threshold, ΔK_{th}, for most stainless steels (6 $MNm^{-3/2}$ or 5.5 $ksi\sqrt{in}$). Furthermore, the plots of the largest principal stress near the seam-weld indicate that, for all four cases, the weld notch is always loaded in compression. As previously stated, crack propagation will not occur in a compressive stress field.

4.5 Comments on Startup Stresses

The calculations presented in the preceding section indicate that a crack will not propagate into the seam-weld under load conditions cycling between off-sun and on-sun operation. However, the shell analyses indicated that the most severe stress condition at the seam-weld occurred during Step 3 of startup. Much can be inferred by comparing the shell results to the steady state continuum results. The steady state continuum-element results demonstrate that the seam-weld remains in compression. This was also observed in the shell calculations, as shown in Figure 12. During startup (Figure 11), the shell calculations indicate that the meridional and circumferential stresses near the *inner* surface of the seam-weld are also in compression, on the order of 70 MPa. Although this is significantly higher than the steady state results, the continuum calculations indicate that (1) the stresses are still too small to raise the J-integral values appreciably, and (2) the compressive stress field, though higher, is not conducive to crack growth.

Moreover, the results of the more detailed seam-weld analysis indicate that the structural load, as opposed to the thermal loads, determine the stress state at the crack tip. Since the four load cases presented span the operating pressure range and the receiver operates within this range during startup, it reasons that the results of these calculations should bound the startup conditions as well.

5 Conclusions

Coupled thermal-structural analyses of the reflux pool-boiler receiver were performed to characterize the operating stress state and to address issues affecting the service life of the receiver. Shell analyses provided information for receiver material selection and design optimization. More detailed continuum element analyses were performed to assess the vulnerability of the seam-weld to fatigue crack growth. Based on these calculations, the following conclusions are made:

- Maximum stresses in the receiver occur 2 minutes into startup (Step 3) due to the uneven temperature distribution across the receiver surface. The stress levels during startup could be reduced if temperatures across the receiver surface could be maintained at a more uniform level.

- Stresses in the 316L SS prototype receiver are near the 100 MPa yield strength of this alloy.

- Because of its higher yield strength, the largest effective stress in the Haynes 230 receiver is less than 39 percent of yield.

- Reducing the aft dome thickness to 1.59 mm reduces the maximum stress in the receiver by over 25 percent. A further reduction to 0.813 mm has a small effect on the overall stress profile; however, the seam-weld stresses decrease another 40 percent. A reduction in aft dome thickness to one closer to the absorber thickness should be considered for the next-generation receiver design.

- The stress distribution near the seam-weld notch depends primarily on the structural load created by the pressure difference between the sodium and the surrounding environment rather than the thermal loads due to temperature cycling. Thus, investigations of the seam-weld fatigue toughness need only consider the range of operating pressures between off-sun and on-sun operation.

- The stress intensity factor, computed using the J-integral method and crack opening-displacement field equations, is significantly below the fatigue threshold for most steels. Furthermore, the crack is always loaded in compression which is not conducive to fatigue crack growth. As a result, the candidate seam-weld investigated in these calculations will not adversely affect the receiver service life.

6 References

1 R. B. Diver, C. E. Andraka, J. B. Moreno, D. R. Adkins, and T. A. Moss, *Trends in Dish-Stirling Solar Receiver Designs*, Sandia National Laboratories, SAND90-1236C; 25th Intersociety Energy Conversion Engineering Conference, Reno, Nevada; August, 1990.

2 C. E. Andraka, J. B. Moreno, R. B. Diver, V. Dudley, and K. S. Rawlinson, *Reflux Pool-Boiler as a Heat-Transport Device for Stirling Engines: On-Sun Test Program Results*, Sandia National Laboratories, SAND89-0268C; 25th Intersociety Energy Conversion Engineering Conference, Reno, Nevada; August, 1990.

3 M. K. Neilsen, *Solar Receiver Thermal Stress Analysis*, memo to J. B. Moreno, Sandia National Laboratories, September 18, 1989.

4 C. M. Stone and E. L. Hoffman, *Thermal Stress Analysis of a Sodium Reflux Pool-Boiler Receiver*, memo to J. B. Moreno, Sandia National Laboratories, October 3, 1990.

5 E. L. Hoffman and C. M. Stone, *Thermal Stress Analysis of a Sodium Reflux Pool-Boiler Receiver Studying the Effects of Nonlinear Material Properties and Reduced Aft Dome Thickness*, memo to J. B. Moreno, Sandia National Laboratories, November 29, 1990.

6 E. L. Hoffman, C. M. Stone, and G. W. Wellman, *Fatigue-Crack Analysis of a Seam Weld in the Reflux Pool Boiler Receiver*, memo to J. B. Moreno, Sandia National Laboratories, January 17, 1991.

7 Hibbitt, Karlsson, and Sorensen, *ABAQUS User's Manual*, Version 4.8, HKS Inc., 1989.

8 J. B. Moreno, C. E. Andraka, R. B. Diver, W. C. Ginn, V. Dudley, and K. S. Rawlinson, *Test Results from a Full-Scale Sodium Reflux Pool-Boiler Solar Receiver*, ASME Solar Energy Division Conference, Miami, Florida, April, 1990.

9 J. B. Moreno and C. E. Andraka, *Review of Sodium Pool Boiler Design*, memo to Distribution, February 8, 1990.

10 *Sodium NaK Engineering Handbook Vol. 1*, O. J. Faust (ed), Gordon and Breach, 1972.

11 A. C. Ratzel and B. D. Boughton, *Circe.001: A computer Code for Analysis of Point-Focus Concentrators with Flat Targets*, SAND86-1866, Sandia National Laboratories, 1986.

12 S. T. Rolfe and J. M. Barsom, *Fracture and Fatigue Control in Structures*, Prentice-Hall Inc.; Englewood Cliffs, NJ, 1977.

13 M. F. Kanninen and C. H. Popelar, *Advanced Fracture Mechanics*, Oxford University Press; New York, NY, 1985.

14 Hibbitt, Karlsson, and Sorensen, *ABAQUS Theory Manual*, Version 4.8, HKS Inc., 1989.

15 A. P. Gilkey and J. H. Glick, *BLOT - A Mesh and Curve Plot Program for the Output of a Finite Element Analysis*, SAND88-1432, June 1989.

Distribution:

U.S. Department of Energy (5)
Forrestal Building
Code CE-132
1000 Independence Avenue, SW
Washington, DC 20585
Attn: M. Scheve
S. Gronich

U.S. Department of Energy (2)
Forrestal Building
Code CE-13
1000 Independence Avenue, SW
Washington, DC 20585
Attn: R. Annan

U.S. Department of Energy (2)
Albuquerque Operations Office
P.O. Box 5400
Albuquerque, NM 87115
Attn: G. Tennyson
N. Lackey

U.S. Department of Energy
San Francisco Operations Office
1333 Broadway
Oakland, CA 94612
Attn: R. Hughey

Acurex Corporation (2)
555 Clyde Avenue
Mountain View, CA 94039
Attn: J. Schaefer
H. Dehne

Advanced Thermal Systems
7600 East Arapahoe
Suite 319
Englewood, CO 80112
Attn: D. Gorman

Arizona Public Service Company
P.O. Box 21666
Phoenix, AZ 85036
Attn: J. McGuirk

Arizona Solar Energy Office
Dept. of Commerce
1700 W. Washington, 5th Floor
Phoenix, AZ 85007
Attn: F. Mancini

Australian National University
Department of Engineering
Physics
P. O. Box 4
Canberra ACT 2600 AUSTRALIA
Attn: S. Kaneff

Barber-Nichols Engineering
6325 West 55th Avenue
Arvada, CO 80002
Attn: R. Barber

Battelle Pacific Northwest Laboratory (2)
P.O. Box 999
Richland, WA 99352
Attn: T. A. Williams
D. Brown

BDM Coporation
1801 Randolph Street
Albuquerque, NM 87106
Attn: W. Schwinkendorf

Bechtel National, Inc. (2)
50 Beale Street
50/15 D8
P. O. Box 3965
San Francisco, CA 94106
Attn: P. DeLaquil
S. Nickovich

Black & Veatch Consulting Engineers
P.O. Box 8405
Kansas City, MO 64114
Attn: J. C. Grosskreutz

Tom Brumleve
1512 Northgate Road
Walnut Creek, CA 94598

California Energy Commission
1516 Ninth Street, M-S 43
Sacramento, CA 95814
Attn: A. Jenkins

California Polytechnic University
Dept. of Mechanical Engineering
Pomona, CA 91768
Attn: W. Stine

California Public Utilities Com.
Resource Branch, Room 5198
455 Golden Gate Avenue
San Francisco, CA 94102
Attn: T. Thompson

Cummins Engine Co. (2)
MC 60125
P. O. Box 3005
Columbus, IN 47202-3005
Attn: R. Kubo

Dan Ka
3905 South Mariposa
Englewood, CO 80110
Attn: D. Sallis

DLR
Pfaffenwaldring 38-40
7000 Stuttgart 80 GERMANY
Attn: R. Buck

Electric Power Research Institute
P.O. Box 10412
Palo Alto, CA 94303
Attn: J. Schaeffer

Energy Research Centre (2)
R. S. Phy. Sc.
Australian National University
Canberra ACT 2601 AUSTRALIA
Attn: K. Inall

Energy Technology Engr. Center
Rockwell International Corp.
P. O. Box 1449
Canoga Park, CA 91304
Attn: W. Bigelow

ENTECH, Inc.
P. O. Box 612246
DFW Airport, TX 75261
Attn: R. Walters

Florida Solar Energy Center
300 State Road 401
Cape Canaveral, FL 32920
Attn: Library

Ford Aerospace
Ford Road
Newport Beach, CA 92663
Attn: R. Babbe

Foster Wheeler Solar Development Corporation (2)
12 Peach Tree Hill Road
Livingston, NJ 07039
Attn: M. Garber
R. Zoschak

Garrett Turbine Engine Co.
111 South 34th Street
P. O. Box 5217
Phoenix, AZ 85010
Attn: E. Strain

Georgia Power (2)
7 Solar Circle
Shenandoah, GA 30265
Attn: W. King

Harris Corporation (2)
Government and Aerospace Systems Division
P. O. Box 9400
Melbourne, FL 32902
Attn: K. Schumacher

Industrial Solar Technologies
5775 West 52nd Avenue
Denver, CO 80212
Attn: R. Gee

Institute of Gas Technology
34245 State Street
Chicago, IL 60616
Attn: Library

Jet Propulsion Laboratory
4800 Oak Grove Drive
Pasadena, CA 91109
Attn: M. Alper

LaJet Energy Company (2)
P. O. Box 3599
Abilene, TX 79604
Attn: M. McGlaun

L'Garde, Inc. (2)
1555 Placentia Avenue
Newport Beach, CA 92663
Attn: M. Thomas
J. Williams

Lawrence Berkeley Laboratory
MS 90-2024
One Cyclotron Road
Berkeley, CA 94720
Attn: A. Hunt

Luz International (2)
924 Westwood Blvd.
Los Angeles, CA 90024
Attn: D. Kearney

3M-Energy Control Products (2)
207-1W 3M Center
St. Paul, MN 55144
Attn: R. Dahlen

McDonnell-Douglas Astronautics Company (3)
5301 Bolsa Avenue
Huntington Beach, CA 92647
Attn: R. L. Gervais,
J. Rogan,
D. Steinmeyer

Mechanical Technology, Inc. (2)
968 Albany Shaker Road
Latham, NY 12110
Attn: G. Dochat
J. Wagner

Meridian Corporation
4300 King Street
Alexandria, VA 22302
Attn: D. Kumar

NASA Lewis Research Center (4)
21000 Brook Park Road
Cleveland, OH 44135
Attn: R. Shaltens
J. Schrieber

Nevada Power Co.
P. O. Box 230
Las Vegas, NV 89151
Attn: Mark Shank

New Mexico Solar Energy Institute
New Mexico State University
Box 3SOL
Las Cruces, NM 88003

Northern Research and Engineering Corp.
39 Olympia Avenue
Woburn, MA 01801-2073
Attn: J. Kesseli

Pacific Gas and Electric Company (2)
3400 Crow Canyon Road
San Ramon, CA 94526
Attn: G. Braun
J. Iannucci

Power Kinetics, Inc. (10)
415 River Street
Troy, NY 12180-2822
Attn: W. E. Rogers

Renewable Energy Institute
1001 Connecticut Ave. NW
Suite 719
Washington, DC 20036
Attn: K. Porter

Rocketdyne Division
6633 Canoga Park Ave.
Canoga Park, CA 91304
Attn: W. Marlatt

San Diego Gas and Electric Company
P.O. Box 1831
San Diego, CA 92112
Attn: R. Figueroa

Southern California Edison (3)
P. O. Box 800
Rosemead, CA 91770
Attn: P. Skvarna

Schlaich, Bergermann & Partner
Hohenzollernstr. 1
D - 7000 Stuttgart 1 GERMANY
Attn: W. Schiel

Sci-Tech International
Advanced Alternative Energy Solutions
5673 W. Las Positas Boulevard
Suite 205
P.O. Box 5246
Pleasanton, CA 84566
Attn: U. Ortabasi

Science Applications International Corporation (2)
10343 Roselle Street, Suite G
San Diego, CA 92121
Attn: K. Beninga

Solar Energy Industries Assoc. (2)
777 North Capitol St. NE
Suite 805
Washington, D.C. 20002
Attn: S. Sklar
K. Sheinkopf

Solar Energy Research Institute (6)
1617 Cole Boulevard
Golden, CO 80401
Attn: B. Gupta
L. M. Murphy
G. Jorgensen
T. Wendelin
A. Lewandowski
M. Bohn

Solar Kinetics, Inc. (2)
P.O. Box 540636
Dallas, TX 75354-0636
Attn: J. A. Hutchison
P. Schertz

Solar Power Engineering Company
P.O. Box 91
Morrison, CO 80465
Attn: H. Wroton

Solar Steam
P. O. Box 32
Fox Island, WA 98333
Attn: D. Wood

SRS Technologies
990 Explorer Blvd., NW
Huntsville, AL 35806
Attn: R. Bradford

Stirling Technology Company (2)
2952 George Washington Way
Richland, WA 99352
Attn: Mr. Maurice A. White

Stirling Thermal Motors
2841 Boardwalk
Ann Arbor, MI 48104
Attn: T. Godett

Sunpower, Inc.
6 Byard Street
Athens, OH 45701
Attn: W. Beale

Tom Tracey
6922 South Adams Way
Littleton, CO 80122

Thermacore, Inc. (2)
780 Eden Road
Lancaster, PA 17601
Attn: Mr. Donald Ernst

United Solar Tech, Inc.
3434 Martin Way
Olympia, WA 98506
Attn: R. Kelley

University of Chicago
Enrico Fermi Institute
5640 Ellis Avenue
Chicago, IL 60637
Attn: J. O'Gallagher

University of Houston
Solar Energy Laboratory
4800 Calhoun
Houston, TX 77704
Attn: L. Vant-Hull
J. Richardson

University of Minnesota
Dept. of Mechanical Engineering
111 Church St., SE
Minneapolis, MN 55455
Attn: E. A. Fletcher

University of New Mexico (2)
Dept. of Mechanical Engineering
Albuquerque, NM 87131
Attn: M. W. Wilden
W. A. Gross

University of Utah
Mechanical and Industrial Engineering
Salt Lake City, UT 84112
Attn: B. Boehm

Eric Weber
302 Caribbean Lane
Phoenix, AZ 85022

WG Associates
6607 Stonebrook Circle
Dallas, TX 75240
Attn: V. Goldberg

Sandia Internal Distribution:

1425 J. H. Biffle
1510 J. C. Cummings
1511 J. S. Rottler
1512 A. C. Ratzel
1513 D. R. Adkins
1513 R. D. Skocypec
1514 H. S. Morgan
1514 E. L. Hoffman (10)
1514 M. K. Neilsen
1514 C. M. Stone
1514 G. W. Wellman
1500A L. W. Davison
1540 J. R. Asay
1544 J. R. Asay (Actg.)
1545 D. R. Martinez
1550 C. W. Peterson
1832 J. A. Van Den Avyle
1833 G. A. Knorovsky
1840 R. E. Loehman
1846 D. H. Doughty
1846 C. S. Ashley
3141-1 S. A. Landenberger (5)
3151 G. C. Claycomb (3)
3145 Document Processing for DOE/ OSTI (8)
6000 V. L. Dugan, Acting
6200 B. W. Marshall, Acting
6210 J. T. Holmes, Acting
6215 A. A. Heckes
6215 C. P. Cameron, Actg (25)
6215 K. S. Rawlinson
6216 C. E. Tyner
6216 D. J. Alpert
6216 T. R. Mancini
6217 C. E. Andraka
6217 P. C. Klimas
6217 R. B. Diver
6217 J. B. Moreno
6220 D. G. Schueler
6223 G. J. Jones
6224 A. R. Mahoney
7470 J. L. Ledman
7476 F. P. Gerstle
7476 S. T. Reed
8523-2 Central Technical Files
8524 J. A. Wackerly

U.S. GOVERNMENT PRINTING OFFICE 1991—673-122 60004

END

DATE FILMED

12/02/91